A coupled nonlinear long-term consolidation and solute transport model for PVD-enhanced flushing remediation analysis of multi-layered contaminated soils

By

Peng-Lin LI, Research Assistant
Department of Civil and Environmental Engineering,
The Hong Kong Polytechnic University, Hung Hom, Kowloon, Hong Kong, China.
Email: pengl.li@connect.polyu.hk

Zhen-Yu YIN, Professor
Department of Civil and Environmental Engineering,
The Hong Kong Polytechnic University, Hung Hom, Kowloon, Hong Kong, China.
Email: zhenyu.yin@polyu.edu.hk
Corresponding author, Tel: +852 3400 8470; Fax: +852 2334 6389

Ding-Bao SONG, Research Assistant Professor
Department of Civil and Environmental Engineering,
The Hong Kong Polytechnic University, Hung Hom, Kowloon, Hong Kong, China.
Email: dingbao.song@polyu.edu.hk

Jian-Hua YIN, Chair Professor
College of Civil and Transportation Engineering,
Shenzhen University, Nanshan District, Shenzhen, China.
Email: jian-hua.yin@polyu.edu.hk

Revised manuscript submitted to *Canadian Geotechnical Journal*

August 10, 2025

Abstract: The remediation of contaminated fine-grained soils through flushing, enhanced by prefabricated vertical drains (PVDs), involves a complex coupled process of axisymmetric consolidation and solute transport. However, existing models often oversimplify these interactions and fail to accurately capture real vacuum pressure boundary conditions. This study presents a coupled nonlinear model that integrates PVD-assisted consolidation and solute transport for multilayered contaminated soils. The governing equations are solved using the finite difference method, and the numerical solution is validated against first analytical solutions for simplified axisymmetric models, then soil-flushing experiments and consolidation-induced solute transport tests. Furthermore, the developed model is applied to assess the effects of key engineering design parameters, including vacuum pressure in PVD, PVD spacing, and PVD penetration length, on cleanup efficiency. Parametric analyses indicate that increasing vacuum pressure and reducing the PVD spacing can improve the cleanup efficiency along the radial direction. However, the treatment depth cannot be significantly enhanced by merely increasing vacuum pressure or reducing the PVD spacings. These findings provide insights into optimizing the design of PVD-enhanced soil flushing systems.

Keywords: Nonlinear consolidation; Solute transport; Prefabricated vertical drains; Vacuum loading

1 Introduction

The combination of prefabricated vertical drains (PVD) and vacuum pressure has been proven to be an effective technique for accelerating the consolidation of fine-grained soils by shortening the seepage path (Chu et al., 2000, 2006; Fox et al., 2003; Chai et al., 2005; Indraratna et al., 2012; Baral et al., 2021). Based on this advantage, the PVD-assisted soil flushing system-featuring injection prefabricated vertical wells (IPVW) and extraction prefabricated vertical wells (EPVW)-has proven highly effective in enhancing the flushing efficiency of contaminated soils as shown in Figure 1 (Gabr et al., 1996a, 1996b; Quaranta et al., 2005; Sharmin et al., 2008; Wu et al., 2024).

To evaluate the efficiency and provide design guidance for PVD-assisted soil flushing systems targeting contaminated soils, various solute transport models and their corresponding analytical solutions have been developed. Gabr et al. (1996a) were among the pioneers in proposing a PVD-enhanced solute transport model to predict the PVD-assisted soil flushing process. The model is based on key assumptions, including an infinite EPVW boundary and a zero-solute concentration boundary at both the IPVW and EPVW interfaces. Evidently, these two assumptions considerably deviate from real-world conditions. On one hand, the assumption of an infinite EPVW boundary suggests that the treatment effectiveness of a PVD-assisted soil flushing system remains unchanged, regardless of the distance between the injection and extraction wells. This assumption is unsuitable for scenarios involving short IPVW-EPVW separations. On the other hand, at the IPVW boundary adjacent to the contaminated soil, solute transport occurs predominantly through advection, with

hydrodynamic dispersion replenishing contaminants from regions of higher concentration. The contaminant concentration gradually decreases, asymptotically approaching zero at the IPVW boundary. Consequently, the assumption of a contaminant-free IPVW boundary becomes invalid. Wang et al. (2014) incorporated a finite EPVW boundary and accounted for the influence of the smear zones induced by PVD installation in the flushing analysis, focusing exclusively on radial solute transport. Additionally, Tang et al. (2015) proposed a planar two-dimensional (2D) analytical model for contaminant extraction using a grid-patterned PVD-enhanced soil flushing system. This model incorporated a finite EPVW boundary and employed a flux-type injection boundary, replacing the zero-solute concentration Dirichlet boundary. Wang et al. (2016) derived an analytical solution for a two-dimensional axisymmetric model to simulate solute transport in a circular IPVW-EPVW configuration.

Previous models employed flux-type injection boundaries as simplified representations of the actual vacuum pressure applied in IPVW and EPVW. Consequently, the flux-type injection boundary fails to faithfully represent the true conditions of vacuum pressure application. Furthermore, these models presume that the water flow velocity, driven by the pore water pressure gradient, remains constant both spatially and temporally. However, the pore pressure distribution arising from consolidation exhibits both spatial and temporal variability. Numerous studies have emphasized the substantial influence of consolidation on solute transport (Alshawabkeh et al., 2004, Lee et al., 2009, Lee and Fox, 2009; Zhang et al., 2025). On one hand, water flow induced by consolidation serves as a primary driving force for convective solute transfer (Nassar and Horton, 1992). Potter et al. (1994) initially proposed a

numerical solution that couples the Terzaghi consolidation equation with the advection-dispersion equation. Since then, various numerical solutions have been developed utilizing the finite element method (Nomura et al., 2018) and the finite difference method (Peter and Smith, 2002). Pu et al. (2020) integrated one-dimensional (1D) self-weight consolidation with advection-dispersion while incorporating nonlinear compressibility and permeability. Additionally, Fox (2007) reported both the theoretical and numerical development of the piecewise-linear Consolidation Solute Transport 1 (CST1) model for coupling large-strain consolidation with solute transport in saturated porous media. Building on the CST1 model, Fox and Lee (2008) and Pu and Fox (2016) introduced the numerical models Consolidation Solute Transport 2 (CST2) model, which incorporates nonlinear and nonequilibrium sorption, and Consolidation Solute Transport 3 (CST3) model for layered soils. Li et al. (2022) and Jiang et al. (2023) further extended to develop the coupled model for nonlinear consolidation and organic solute transport. On the other hand, consolidation induces nonlinear variations in both consolidation and solute transport parameters (Lee et al., 2009, Lee and Fox, 2009), such as the compression index, permeability coefficient, and diffusion coefficient. These parameters are crucial determinants of solute transport and clean-up efficiency. These studies predominantly focus on 1D conditions. Key features of PVD-assisted consolidation, including radial water flow, the smear zone effect due to PVD installation (Walker and Indraratna, 2006; Wang et al., 2014; Prabavathy et al., 2021), and the discharge capacity of PVD along depth (Bergado et al., 1996; Miura and Chai, 2000; Bo et al., 2016; Nguyen and Kim, 2019), have not been incorporated into these 1D consolidation and solute transport coupling models.

Ignoring these factors may lead to inaccurate predictions of the coupled process, potentially resulting in misleading guidance for practical engineering design. Notably, several comprehensive PVD-assisted consolidation models that incorporate key influencing factors have been developed. However, the extension of comprehensive models for soil flushing analysis remains underdeveloped (Li et al., 2022; Jiang et al., 2023; Huangfu and Deng, 2024). Current studies used for soil flushing analysis still ignored the coupling of PVD-assisted consolidation, as shown Table 1.. Only Huangfu and Deng (2024) have developed a PVD-assisted consolidation-solute transport model under 2D plane strain conditions, considering nonlinear consolidation in fully or partially saturated, as well as less to highly deformable, and permeable to impermeable layers. Therefore, extending the existing axisymmetric PVD-assisted consolidation model to couple solute transport is essential for analyzing the soil flushing process. In this way, real conditions of the soil flushing process, including vacuum pressure boundaries, nonuniform water flow velocity along the radial direction, and PVD-induced issues such as the smear zone, can be integrated into engineering design. A comprehensive model has broader applicability for soils exhibiting strong consolidation effects (e.g., clay slurry) or weak consolidation effects (e.g., high-density soils).

To fill the abovementioned research gaps, this study aims to develop an axisymmetric model coupling the solute transport and PVD-assisted consolidation for flushing analysis of multilayered contaminated soils. Firstly, the model was developed by deriving the PVD-assisted consolidation equations, considering creep, smear zone, nonlinearly variable hydraulic conductivity, and vacuum loading. The axisymmetric solute transport model was then

established and incorporated into the consolidation model to form the fully coupled model. This approach enables the simulation of more realistic engineering conditions. The efficiency of the proposed model is verified by being compared with analytical models and test data. Finally, parametric studies are conducted to explore the effect of several engineering concerns factors, including vacuum pressure values within the PVD, PVD spacing, and PVD length, on the PVD-enhanced soil flushing efficiency.

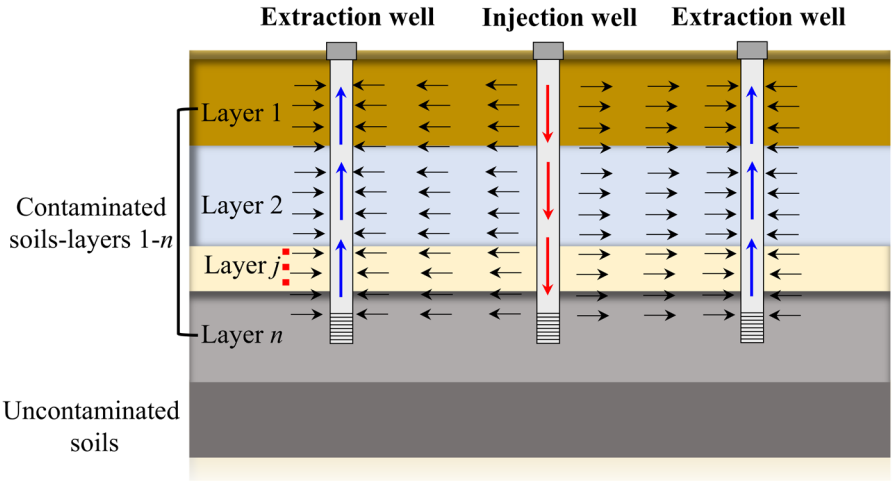

Figure 1 Schematic diagram of using flushing system to accelerate the clean-up of contaminated soil ground

Table 1 Existing solute transport models for contaminated soils

Authors	Factors included					
	Vertical direction water flow	Radial direction water flow	Smear zone	Nonlinear consolidation	Real vacuum pressure boundary	Creep
Gabr et al. (1996a)	N	Y	N	N	N (zero-solute concentration Dirichlet boundary)	N
Wang et al. (2014)	N	Y	Y	N	N (zero-solute concentration Dirichlet boundary)	N
Tang et al. (2015)	Y	Y	N	Y	N (flux-type injection boundary)	N

Wang et al. (2016)	N	Y	N	Y	N (flux-type injection boundary)	N
Potter et al. (1994)	Y	N	N	N	-	N
Pu et al. (2020)	Y	N	N	Y	-	N
Fox (2007)	Y	N	N	Y	-	N
Fox and Lee (2008)	Y	N	N	Y	-	N
Pu and Fox (2016)	Y	N	N	Y	-	N
Li et al. (2022)	Y	N	N	Y	-	N
Jiang et al. (2023)	Y	N	N	Y	-	N
Huangfu and Deng (2024)	Y	N (2D plane strain)	Y	Y	Y	N
This study	Y	Y	Y	Y	Y	Y

Note: Y = considered; N = Not considered.

2 Model description

The governing equations are derived based on the following assumptions: (a) The soil is fully saturated; (b) Both pore solution and soil particles are incompressible; (c) The pore solution flow obeys Darcy's law; (d) Strain occurs only in the vertical direction, while pore water flow takes place in both vertical and radial direction. This assumption has been widely adopted and validated as applicable for analyzing PVD-assisted consolidation processes (Geng et al., 2017; Nguyen et al., 2019); (e) Solute transport occurs in both vertical and radial directions; (f) Adsorption is assumed to be linear; (g) Biodegradation or non-equilibrium

adsorption is not considered.

2.1 Coordinate Systems

The multi-layered PVD-enhanced contaminated soil ground with injection and exaction wells can be simplified to an axisymmetric unit cell, as shown in Figure 2, described in the Lagrangian coordinate (Figure 2(a)) and Convective coordinate Figure 2(b), respectively. Two coordinate systems can convert each other by the relationship (Gibson et al., 1967, 1981):

$$\frac{\partial \xi}{\partial a} = \frac{1+e}{1+e_0} \tag{1}$$

where e is the current void ratio of the position at (r, a); e_0 is the initial void ratio of the soil.

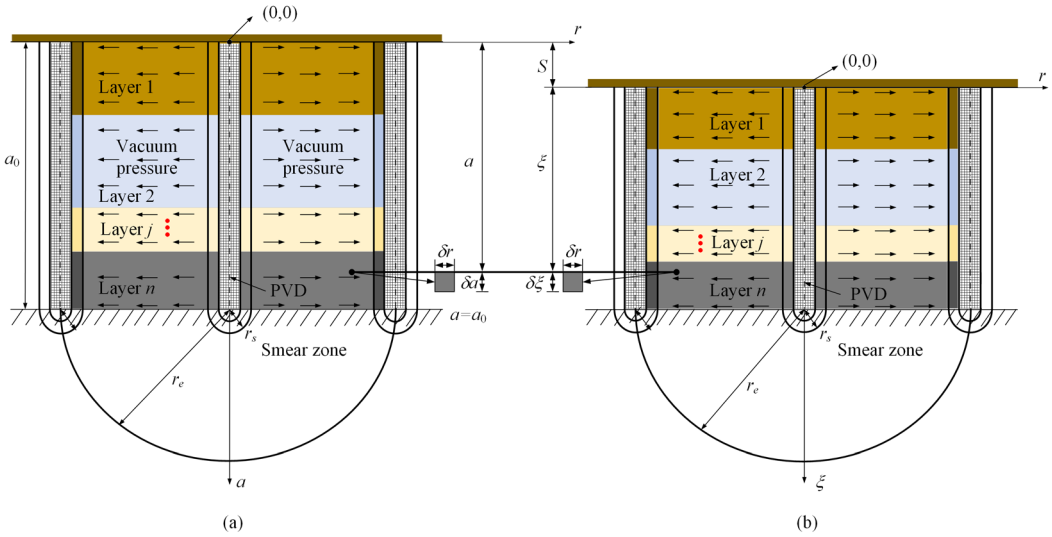

Figure 2 Coordinate systems for the axisymmetric unit cell: (a) Lagrangian coordinate a; (b) Convective coordinate ξ

2.2 Axisymmetric finite strain consolidation model

Stress equilibrium condition

Considering a current infinitesimal element of vertical stress equilibrium of soil particles

in Convective coordinate in the *j*th layer, the stress equilibrium can be expressed as follows:

$$\frac{\partial \sigma_j(\xi,r,t)}{\partial \xi} = \gamma_{m,j} = \frac{G_{s,j}+e_j}{1+e_j}\gamma_w \tag{2}$$

where σ is the total vertical stress; γ_m is the unit weight of saturated soil; G_s is the specific gravity of the soil particle; γ_w is the unit weight of water; the subscript is the layer number.

In the radial direction, the stress equilibrium of soil particles follows:

$$\frac{\partial \sigma_j(\xi,r,t)}{\partial r} = 0 \tag{3}$$

Pore water flow

In the vertical direction, the relationship between total pore water pressure and excess pore water pressure is:

$$\frac{\partial u_{w,j}}{\partial \xi} = \frac{\partial\left(u_{e,j}+u_{h,j}\right)}{\partial \xi} = \frac{\partial u_{e,j}}{\partial \xi} + \gamma_w \tag{4}$$

where u_w is the total pore water pressure; u_e is the excess pore water pressure; u_h is the hydrostatic pressure.

Hydrostatic pressure is independent of positions in radial direction, i.e., $\partial u_{h,j} / \partial r = 0$, and therefore,

$$\frac{\partial u_{w,j}}{\partial r} = \frac{\partial u_{e,j}}{\partial r} \tag{5}$$

Then the relative velocity of the fluid and solid phases in the vertical direction can be conveyed using the excess pore water pressure u_e:

$$n\left(v_{w,j}-v_{s,j}\right) = -k_{v,j}\left(\frac{1}{\gamma_w}\frac{\partial u_{e,j}}{\partial \xi}\right) \tag{6}$$

where n is the porosity, v_w and v_s are the velocities of fluid and solid phases in the vertical direction, respectively.

Similarly, the relative velocity in the radial direction is:

$$nv_{r,j} = -k_{r,j}\left(\frac{1}{\gamma_w}\frac{\partial u_{e,j}}{\partial r}\right) \tag{7}$$

The void ratio-dependent permeability coefficient was adopted as below:

$$k_{v,j} = k_{v0,j}\left(1+e_j\right)^{n_{v,j}} \tag{8}$$

$$k_{r,j} = k_{r0,j}\left(1+e_j\right)^{n_{r,j}} \tag{9}$$

where k_{v0}, n_v, k_{r0}, and n_r are vertical and radial permeability coefficient parameters. It should be noted that the symbols k_{v0} and k_{r0} denote the permeability coefficients when e=0.

A differential soil element in a cylindrical coordinate system, as depicted in Figure 3, is considered. In this system, pore water movement is permitted in both radial and vertical directions, while no flow occurs in the θ-direction.

Continuity equation

According to the continuity condition, the volume change rate of the soil element, $\partial V_j / \partial t$, is equal to the difference between the water amount of flow into and out of the element in the unit time period, Δq_j:

$$\frac{\partial V_j}{\partial t} = \frac{\partial q_{r,j}}{\partial r}dr + \frac{\partial q_{\xi,j}}{\partial \xi}d\xi \tag{10}$$

where q_r is the flow flux in the radial direction; q_ξ is the flow flux in the vertical direction.

The flow flux in the radial direction $q_{r,j}$ can be written as:

$$q_{r,j} = n_j v_{r,j} \left(r d\theta d\xi \right) \tag{11}$$

The flow flux in the vertical direction $q_{\xi,j}$ is:

$$q_{\xi,j} = n_j \left(v_{w,j} - v_{s,j} \right) \left(r d\theta dr \right) \tag{12}$$

Incorporating Equations (11) and (12) into (10), one can have:

$$\frac{\partial V_j}{\partial t} = \frac{\partial \left[v_{r,j} \left(r d\theta d\xi \right) \right]}{\partial r} dr + \frac{\partial \left[\left(v_{w,j} - v_{s,j} \right) \left(r d\theta dr \right) \right]}{\partial \xi} d\xi \tag{13}$$

Based on the assumption that deformation only occurs in the vertical direction, Equation (13) can be rewritten using void ratio (Li et al., 2025):

$$\frac{1}{1+e} \frac{\partial e}{\partial t} = \frac{\partial v_{r,j}}{\partial r} + \frac{v_{r,j}}{r} + \frac{\partial \left(v_{w,j} - v_{s,j} \right)}{\partial \xi} \tag{14}$$

Combining Equations (6), (7), and (14), one can obtain:

$$\frac{1}{1+e_j} \frac{\partial e_j}{\partial t} = \frac{\partial}{\partial r} \left(\frac{k_{r,j}}{\gamma_w} \frac{\partial u_{e,j}}{\partial r} \right) + \frac{k_{r,j}}{r} \left(\frac{1}{\gamma_w} \frac{\partial u_{e,j}}{\partial r} \right) + \frac{\partial}{\partial \xi} \left(\frac{k_{v,j}}{\gamma_w} \frac{\partial u_{e,j}}{\partial \xi} \right) \tag{15}$$

Equation (15) describes the continuity of pore fluid flow in a deforming saturated soil matrix, relating the rate of pore water volume change to the deformation of the soil skeleton and thereby ensuring mass conservation under large-strain conditions.

Constitutive relationship

The Yin-Graham EVP model, a widely recognized model (Yin and Graham, 1989, 1994, 1996), is incorporated into the axisymmetric finite strain consolidation framework. The Yin-Graham EVP model has also been adapted into the extended EVP model for large strain, as follows (Yin and Zhu, 2020; Li et al., 2023):

$$\frac{\partial e_j}{\partial t}=-\kappa\frac{\partial \sigma'_j}{\partial t}\frac{1}{\sigma'_{ref,j}+\sigma'_j}-\frac{\psi_j}{t_{0,j}}\exp\left(\frac{e_j-e^{ep}_{p,j}}{\psi_j}\right)\left(\frac{\sigma'_{ref,j}+\sigma'_j}{\sigma'_{ref,j}+\sigma'_{p,j}}\right)^{\lambda_j/\psi_j} \tag{16}$$

where σ'_{ref} is a reference non-zero small value, which can be taken as 0 to 1 kPa or checked by fitting test data at very small vertical effective stress (e.g., 0 kPa) (Li et al., 2023), to ensure that the expression still makes sense when the effective stress approaches 0. Adding σ'_{ref} to the 1D Yin–Graham EVP model can keep strain from becoming too large or even infinite; κ and λ are the elastic and elastic-plastic compression index in the Cam-clay models, respectively; t_0 and ψ are the parameters related to creep; σ'_p has a somewhat similar role to the pre-consolidation pressure p_c, e^{ep}_{zp} is the void ratio corresponding to σ'_p.

The effective stress principle is expressed as follows:

$$\sigma_j=\sigma'_j+u_{w,j} \tag{17}$$

Substituting Equation (17) into Equation (16), then we can obtain:

$$\frac{\partial e_j}{\partial t}=-\kappa_j\frac{\partial\left(\sigma_j-u_{w,j}\right)/\partial t}{\sigma'_{ref,j}+\left(\sigma_j-u_{w,j}\right)}-\frac{\psi_j}{t_{0,j}}\exp\left(\frac{e_j-e^{ep}_{p,j}}{\psi_j}\right)\left[\frac{\sigma'_{ref,j}+\left(\sigma_j-u_{w,j}\right)}{\sigma'_{ref,j}+\sigma'_{p,j}}\right]^{\lambda_j/\psi_j} \tag{18}$$

Equations (2), (15), and (18) could be rewritten in Lagrangian coordinate as

$$\frac{\partial\sigma_j\left(a,r,t\right)}{\partial a}=\frac{G_{s,j}+e_j}{1+e_0}\gamma_w \tag{19}$$

$$\frac{\partial}{\partial r}\left(\frac{k_{r,j}}{\gamma_w}\frac{\partial u_{e,j}}{\partial r}\right)+\frac{k_{r,j}}{r}\left(\frac{1}{\gamma_w}\frac{\partial u_{e,j}}{\partial r}\right)+\frac{1+e_{0,j}}{1+e_j}\frac{\partial}{\partial a}\left[k_{\xi,j}\left(\frac{1}{\gamma_w}\frac{1+e_{0,j}}{1+e_j}\frac{\partial u_{e,j}}{\partial a}\right)\right]=\frac{1}{1+e_j}\frac{\partial e_j}{\partial t} \tag{20}$$

$$\frac{\partial e_j}{\partial t}=-m_{v,j}\left(u_w,\sigma\right)\frac{\partial\left(\sigma_j-u_{w,j}\right)}{\partial t}-g_j\left(u_w,e,\sigma\right) \tag{21}$$

where:

$$m_{v,j}\left(u_w,\sigma\right)=\frac{\kappa_j}{\sigma'_{ref,j}+\left(\sigma_j-u_{w,j}\right)} \tag{22}$$

$$g_j\left(u_w,e,\sigma\right)=\frac{\psi_j}{t_{0,j}}\exp\left(\frac{e_j-e_{p,j}^{ep}}{\psi_j}\right)\left[\frac{\sigma'_{ref,j}+\left(\sigma_j-u_{w,j}\right)}{\sigma'_{ref,j}+\sigma'_{p,j}}\right]^{\lambda_j/\psi_j} \tag{23}$$

To obtain the excess pore water pressure u_e directly, here we introduce

$$\sigma_j=\sigma_{ah,j}+u_{h,j} \tag{24}$$

where σ_{ah} is the total stress above hydrostatic pressure.

Then the effective stress can be expressed by the following equation:

$$\sigma'_j=\sigma_{ah,j}-u_{e,j} \tag{25}$$

Using u_e and σ_{ah} instead of u_w and σ respectively, Equations (19)-(23) could also be rewritten as follows:

$$\frac{\partial\sigma_{ah,j}}{\partial a}=\frac{G_{s,j}-1}{1+e_{0,j}}\gamma_w \tag{26}$$

$$\begin{aligned}&\frac{\partial}{\partial r}\left(\frac{k_{r,j}}{\gamma_w}\frac{\partial u_{e,j}}{\partial r}\right)+\frac{1}{r}\left(\frac{k_{r,j}}{\gamma_w}\frac{\partial u_{e,j}}{\partial r}\right)+\frac{1+e_{0,j}}{1+e_j}\frac{\partial}{\partial a}\left(\frac{k_{v,j}}{\gamma_w}\frac{1+e_{0,j}}{1+e_j}\frac{\partial u_{e,j}}{\partial a}\right)\\&=-m_{v,j}\left(u_e,\sigma_{ah}\right)\frac{\partial\left(\sigma_{ah}-u_e\right)}{\partial t}-g\left(u_e,e,\sigma_{ah}\right)\end{aligned} \tag{27}$$

$$\frac{\partial e_j}{\partial t}=-m_{v,j}\left(u_e,\sigma_{ah}\right)\frac{\partial\left(\sigma_{ah,j}-u_{e,j}\right)}{\partial t}-g_j\left(u_e,e,\sigma_{ah}\right) \tag{28}$$

where:

$$m_{v,j}\left(u_e,\sigma_{ah}\right)=\frac{\kappa_j}{\sigma'_{ref,j}+\left(\sigma_{ah,j}-u_{e,j}\right)} \tag{29}$$

$$g_j\left(u_e,e,\sigma_{ah}\right)=\frac{\psi_j}{t_{0,j}}\exp\left(\frac{e_j-e_{p,j}^{ep}}{\psi_j}\right)\left[\frac{\sigma'_{ref,j}+\left(\sigma_{ah,j}-u_{e,j}\right)}{\sigma'_{ref,j}+\sigma'_{p,j}}\right]^{\lambda_j/\psi_j} \tag{30}$$

Equations (26)-(30) formulate the axisymmetric finite strain consolidation model. Equations (27) and (28) are derived by combining the continuity equation with the effective stress principle and the adopted EVP constitutive relationship, establishing the coupling among

229 excess pore pressure, total stress, and void ratio during consolidation. Equations (29) and (30)
230 define two intermediate variables introduced to simplify the expressions of Equations (27) and
231 (28) and to facilitate numerical implementation. These serve as auxiliary formulations to
232 streamline the governing equation system. Collectively, Equations (26)–(28) serve as the
233 primary governing equations for the coupled consolidation process, controlling the evolution
234 of the three key state variables: excess pore water pressure, total stress, and void ratio.

235

236 **2.3 Solute transport governing equations**

237 In this section, the governing equations for solute transport are derived. Initially, within a
238 Representative Volume Element (RVE) such as the soil element in the *j*th layer in Figure 3, the
239 transport amount of solute in the pore solution per unit time can be expressed mathematically
240 as:

241 $$\frac{\partial}{\partial t}\left(n_j r d\theta dr d\xi c_j\right) \tag{31}$$

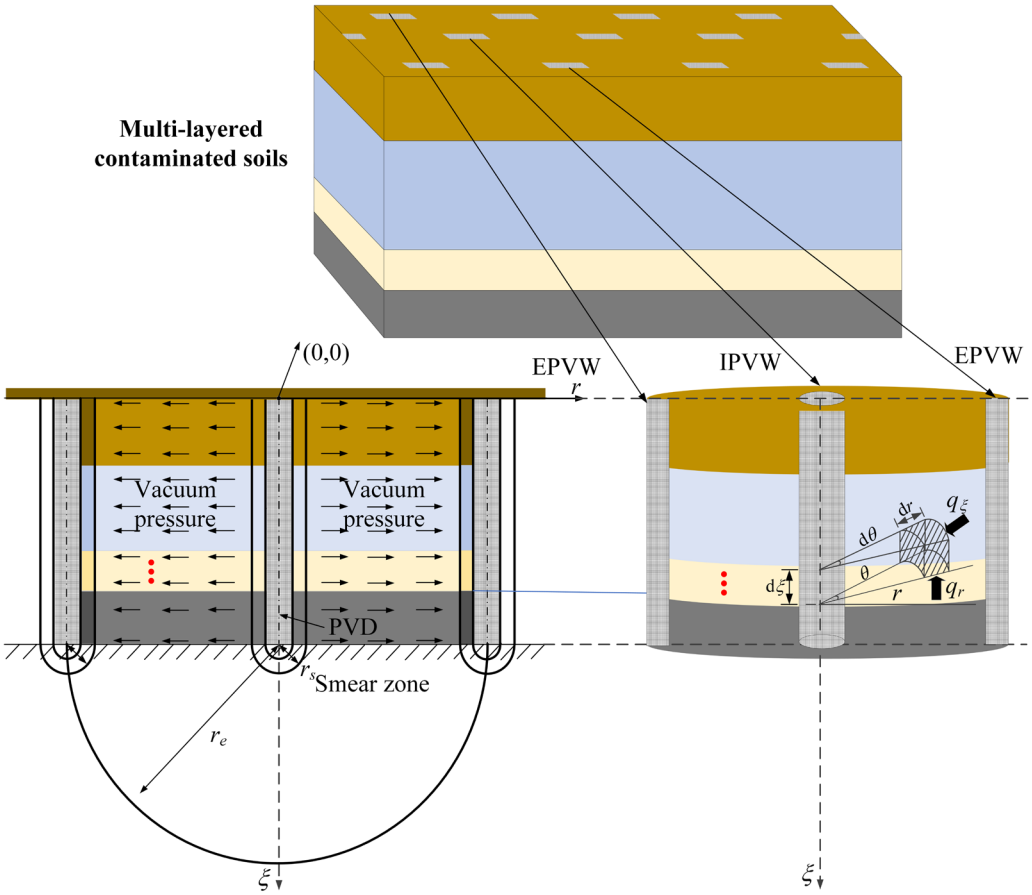

Figure 3 Schematic diagram of axisymmetric composite ground

The solute flux entering the soil element in the *j*th layer unit per unit time is expressed as follows:

$$J_{\xi,j}A_{\xi,j}+J_{r,j}A_{r,j}=\left[n_j\left(v_{w,j}-v_{s,j}\right)c_j-\left(n_jD_{ev,j}\frac{\partial c_j}{\partial \xi}\right)\right]rd\theta dr+\left[\left(n_jv_{r,j}c_j\right)-\left(n_jD_{er,j}\frac{\partial c_j}{\partial r}\right)\right]rd\theta d\xi \quad (32)$$

where D_{ev} is the effective diffusion coefficient in the vertical direction, D_{er} is the effective diffusion coefficient in the radial direction.

The solute flux exiting a soil element per unit time under 2D axisymmetric condition is governed by:

$$\begin{aligned}\left(J_{z,j}+dJ_{z,j}\right)A_{z,j}+\left(J_{r,j}+dJ_{r,j}\right)A_{r,j}&=\left[n_j\left(v_{w,j}-v_{s,j}\right)c_j-\left(n_jD_{ev,j}\frac{\partial c_j}{\partial\xi}\right)\right]rd\theta dr\\&+\frac{\partial}{\partial\xi}\left[n_j\left(v_{w,j}-v_{s,j}\right)c_j-\left(n_jD_{ev,j}\frac{\partial c_j}{\partial\xi}\right)\right]rd\theta drd\xi\\&-\left(n_jv_{r,j}c_j-n_jD_{er,j}\frac{\partial c_j}{\partial r}\right)rd\theta d\xi-\frac{\partial}{\partial r}\left[\left(n_jv_{r,j}c_j-n_jD_{er,j}\frac{\partial c_j}{\partial r}\right)rd\theta d\xi\right]dr\end{aligned}\tag{33}$$

Then, the difference between the inflow and outflow within the soil element can be expressed as follows:

$$\begin{aligned}&-\frac{\partial}{\partial\xi}\left[n_j\left(v_{w,j}-v_{s,j}\right)c_j-\left(n_jD_{ev,j}\frac{\partial c_j}{\partial\xi}\right)\right]d\xi rd\theta dr\\&-\frac{\partial}{\partial r}\left\{\left[\left(n_jv_{r,j}c_j\right)-\left(n_jD_{er,j}\frac{\partial c_j}{\partial r}\right)\right]rd\theta d\xi\right\}dr\end{aligned}\tag{34}$$

According to the mass conservation equation, one can obtain:

$$\begin{aligned}\frac{\partial}{\partial t}\left(n_jrd\theta drd\xi c_j\right)&=-\frac{\partial}{\partial\xi}\left[n_j\left(v_{w,j}-v_{s,j}\right)c_j-\left(n_jD_{ev,j}\frac{\partial c_j}{\partial\xi}\right)\right]rd\theta drd\xi\\&-\frac{\partial}{\partial r}\left[\left(n_jv_{r,j}c_j-n_jD_{er,j}\frac{\partial c_j}{\partial r}\right)rd\theta d\xi\right]dr\end{aligned}\tag{35}$$

Expressing Equation (35) in Lagrangian coordinate, one can obtain:

$$\begin{aligned}\frac{\partial}{\partial t}\left(n_j\frac{1+e_j}{1+e_{0,j}}c_j\right)&=-\frac{\partial}{\partial a}\left[n_j\left(v_{w,j}-v_{s,j}\right)c_j-\left(n_jD_{ev,j}\frac{1+e_{0,j}}{1+e_j}\frac{\partial c_j}{\partial a}\right)\right]\\&-\left[\left(n_jv_{r,j}c_j-n_jD_{er,j}\frac{\partial c_j}{\partial r}\right)\frac{1+e_j}{1+e_{0,j}}\right]\frac{1}{r}-\frac{\partial}{\partial r}\left[\left(n_jv_{r,j}c_j-n_jD_{er,j}\frac{\partial c_j}{\partial r}\right)\frac{1+e_j}{1+e_{0,j}}\right]\end{aligned}\tag{36}$$

Additionally, taking into account that a portion of the solutes is adsorbed onto soil particles, the solutes passing through the REV must adhere to the following mass conservation equation:

$$\frac{\partial}{\partial t}\left[\left(1-n_j\right)c_{s,j}\rho_s\frac{\partial\xi}{\partial a}\right]=f_j\tag{37}$$

where ρ_s is density of soil particle, c_s is the mass of solute adsorbed on soil particles per unit mass, f is the rate of change in mass of solute received by the solid phase from the liquid phase.

Then, one can obtain:

$$\begin{aligned}\frac{\partial}{\partial t}\left(\frac{c_{s,j}\rho_s + e_j c_j}{1+e_{0,j}}\right) &= -\frac{\partial}{\partial a}\left[n_j\left(v_{w,j}-v_{s,j}\right)c_j\right] + \frac{\partial}{\partial a}\left(n_j D_{ev,j}\frac{1+e_{0,j}}{1+e_j}\frac{\partial c_j}{\partial a}\right) \\ &-\left[\left(n_j v_{r,j}c_j - n_j D_{er,j}\frac{\partial c_j}{\partial r}\right)\frac{1+e_j}{1+e_{0,j}}\right]\frac{1}{r} - \frac{\partial}{\partial r}\left[\left(n_j v_{r,j}c_j - n_j D_{er,j}\frac{\partial c_j}{\partial r}\right)\frac{1+e_j}{1+e_{0,j}}\right]\end{aligned} \tag{38}$$

Numerous models have been proposed to characterize the adsorption effect, including nonlinear models such as the widely used Langmuir and Freundlich models, as well as linear models. In this study, a linear, reversible, isothermal adsorption relationship is adopted:

$$c_s = K_d c \tag{39}$$

where K_d is adsorption coefficient.

Incorporating Equation (39), Equation (38) can be expressed as follows:

$$\begin{aligned}\frac{\partial}{\partial t}\left(\frac{K_{d,j}\rho_s + e_j}{1+e_{0,j}}c_j\right) &= -\frac{\partial}{\partial a}\left[n_j\left(v_{w,j}-v_{s,j}\right)c_j\right] + \frac{\partial}{\partial a}\left(n_j D_{ev,j}\frac{1+e_{0,j}}{1+e_j}\frac{\partial c_j}{\partial a}\right) \\ &-\left[\left(n_j v_{r,j}c_j - n_j D_{er,j}\frac{\partial c_j}{\partial r}\right)\frac{1+e_j}{1+e_{0,j}}\right]\frac{1}{r} - \frac{\partial}{\partial r}\left[\left(n_j v_{r,j}c_j - n_j D_{er,j}\frac{\partial c_j}{\partial r}\right)\frac{1+e_j}{1+e_{0,j}}\right]\end{aligned} \tag{40}$$

Although grounded in the classical mass conservation principle (Peter and Smith, 2002; Fox and Lee, 2008; Pu and Fox, 2016), the solute transport equations in this study were independently developed. The model incorporates axisymmetric radial and vertical solute fluxes, void ratio–dependent permeability coefficients, and coupling with large-strain consolidation and smear zone effects, all formulated in a Lagrangian framework for PVD-assisted remediation scenarios.

Equations (26)-(30) and Equation (40) collectively constitute the coupled model for

281 axisymmetric consolidation and solute transport. Unlike conventional solute transport models
282 that typically assume non-deformable soils or purely one-dimensional conditions, the present
283 framework couples axisymmetric consolidation and solute transport under large-strain
284 conditions, dynamically capturing the evolution of pore fluid velocities driven by excess pore
285 pressure dissipation. It incorporates void ratio dependent permeability and linear adsorption for
286 both dissolved and sorbed phases, as in advanced deformable soil transport models such as
287 CST2, and extends the formulation to include radial flow, vacuum pressure boundaries, and
288 smear zone effects, which have rarely been integrated within a single framework. These
289 enhancements significantly improve the model capability to simulate real-world PVD-assisted
290 flushing operations.
291
292 **2.4 Alternating direction implicit (ADI) solution**
293 The general ADI method (Peaceman and Rachford, 1955) to solve 2D highly non-linear
294 partial differential equations (PDEs) was utilized to solve the fully coupled axisymmetric
295 consolidation and solute transport model.
296 To derive the FD schemes of the Equations (27), (28), and (40) more directly, several
297 simplifications were conducted to obtain:
298 $$A_5 \frac{\partial u_e}{\partial t} = \frac{\partial}{\partial r}\left(A_1 \frac{\partial u_e}{\partial r} \right) + A_3 \frac{\partial}{\partial a}\left(A_2 \frac{\partial u_e}{\partial a} \right) + \frac{1}{r}\left(A_1 \frac{\partial u_e}{\partial r} \right) + A_4 \quad (41)$$
299 $$\frac{\partial e}{\partial t} = -A_4 + \frac{\partial u_e}{\partial t} \quad (42)$$
300 $$F_6 \frac{\partial c}{\partial t} = \frac{\partial}{\partial r}\left(F_1 \frac{\partial c}{\partial r} \right) + \frac{\partial}{\partial a}\left(F_2 \frac{\partial c}{\partial a} \right) + \frac{\partial}{\partial r}\left(F_3 c \right) + \frac{\partial}{\partial a}\left(F_4 c \right) + F_1 \frac{\partial c}{\partial r}\frac{1}{r} + F_3 \frac{c}{r} + F_5 \frac{\partial e}{\partial t} \quad (43)$$
301 where:

$$A_1 = \frac{k_r}{\gamma_w} = \frac{k_{r0}\left(1+e\right)^{n_r}}{\gamma_w} \tag{44}$$

$$A_2 = \frac{k_v}{\gamma_w}\frac{1+e_0}{1+e} = \frac{k_{v0}\left(1+e_0\right)\left(1+e\right)^{n_v-1}}{\gamma_w} \tag{45}$$

$$A_3 = \frac{1+e_0}{1+e} \tag{46}$$

$$A_4 = m_v\left(u_e, \sigma_{ah}\right)\frac{\partial \sigma_{ah}}{\partial t} + g\left(u_e, e, \sigma_{ah}\right) \tag{47}$$

$$A_5 = m_v\left(u_e, \sigma_{ah}\right) \tag{48}$$

$$F_1 = \frac{e\left(1+e_0\right)}{\left(1+e\right)^2} D_{er} \tag{49}$$

$$F_2 = \frac{e\left(1+e_0\right)}{\left(1+e\right)^2} D_{ev} \tag{50}$$

$$F_3 = -\frac{e\left(1+e_0\right)}{\left(1+e\right)^2} v_r \tag{51}$$

$$F_4 = -n\left(v_F - v_S\right) = -\frac{k_{v0}\left(1+e\right)^{n_v-1}\left(1+e_0\right)}{\gamma_w}\frac{\partial u_e}{\partial a} \tag{52}$$

$$F_5 = -\frac{c}{1+e_0} \tag{53}$$

$$F_6 = \left(\frac{K_d \rho_s + e}{1+e_0}\right) \tag{54}$$

FD forms of governing equations

The discretization of the time derivative is carried out using the backward difference method:

$$\frac{\partial u_e}{\partial t} = \frac{u_e^{t+\Delta t} - u_e^t}{\Delta t} \tag{55}$$

where Δt the time step size.

To discretize the spatial derivatives, central difference methods were employed in both the *r*-direction and the *a*-direction:

$$\frac{\partial u_e}{\partial r} = \frac{u_{eI,J+1} - u_{eI,J-1}}{2\Delta r} \tag{56}$$

$$\frac{\partial^2 u_e}{\partial r^2} = \frac{u_{eI,J+1} - 2u_{eI,J} + u_{eI,J-1}}{(\Delta r)^2} \tag{57}$$

$$\frac{\partial u_e}{\partial a} = \frac{u_{eI+1,J} - u_{eI-1,J}}{2\Delta a} \tag{58}$$

$$\frac{\partial^2 u_e}{\partial a^2} = \frac{u_{eI+1,J} - 2u_{eI,J} + u_{eI-1,J}}{(\Delta a)^2} \tag{59}$$

where subscripts I and J are the variables along vertical direction and radial direction. Every soil layer is sliced into M and N elements in vertical and radial direction, respectively.

To apply the ADI method, an intermediate step $t + \Delta t/2$ was introduced. In the first step, an implicit scheme for the spatial derivative in the radial direction to obtain the intermediate variable $u_e^{t+\Delta t/2}$ was applied, while using an explicit scheme for the spatial derivative in the vertical direction. The discretized form of Equation (41) is as follows:

$$u_{eI,J}^{t+\Delta t/2} = E^{\mathrm{I}} + E^{\mathrm{II}} u_{eI,J+1}^{t+\Delta t/2} + E^{\mathrm{III}} u_{eI,J-1}^{t+\Delta t/2} \tag{60}$$

where E^{I}, E^{II}, and E^{III} are variables. The detailed description of E^{I}, E^{II}, and E^{III} can be found in Appendix A.

In the second step, the spatial derivative in the vertical direction is computed using an implicit scheme, while the spatial derivative in the radial direction is solved using an explicit scheme. The final discretized form of Equation (41) is expressed as:

$$u_{eI,J}^{t+\Delta t} = F^{\mathrm{I}} + F^{\mathrm{II}} u_{eI+1,J}^{t+\Delta t} + F^{\mathrm{III}} u_{eI-1,J}^{t+\Delta t} \tag{61}$$

where F^{I}, F^{II}, and F^{III} are variables. The detailed description of F^{I}, F^{II}, and F^{III} can be found in Appendix A. More details of the derivation of Equations (60) and (61) are shown in Appendix A.

After updating the excess pore pressure using Equations (60) and (61), the void ratio in the new time step can be calculated as below:

$$e_{I,J}^{t+\Delta t} = -A_4 \Delta t + \left(u_{eI,J}^{t+\Delta t} - u_{eI,J}^{t} \right) + e_{I,J}^{t} \tag{62}$$

Further, the same ADI steps are used to discrete the solute transport governing Equation (43), leading to the following expression::

$$c_{I,J}^{t+\Delta t/2} = M^{\mathrm{I}} + M^{\mathrm{II}} c_{I,J+1}^{t+\Delta t/2} + M^{\mathrm{III}} c_{I,J-1}^{t+\Delta t/2} \tag{63}$$

$$c_{I,J}^{t+\Delta t} = N^{\mathrm{I}} + N^{\mathrm{II}} c_{I+1,J}^{t+\Delta t} + N^{\mathrm{III}} c_{I-1,J}^{t+\Delta t} \tag{64}$$

where M^{I}, M^{II}, M^{III}, N^{I}, N^{II}, and N^{III},are variables analogous to E^{I}, E^{II}, E^{III}, F^{I}, F^{II}, and F^{III} in Equations (60) and (61). The derivations of Equations (63) and (64) follow the same procedure as those of Equations (60) and (61), as detailed in Appendix A. Therefore, the derivation process will not be elaborated on further.

Boundary conditions

In addition, the boundary conditions are significant for solving the PDEs. In this study, boundaries related to consolidation and solute transport are introduced, along with the mathematical formulations and the corresponding engineering conditions in real-world applications.

Regarding the conditions related to consolidation, both the freely drained and undrained states can be represented using the following finite difference formulations:

$$u_{e0,J}^{t} = 0 \ \left(J=1, 2, 3, \ldots, N \right) \tag{65}$$

$$u_{eM,J}^{t} - u_{eM-1,J}^{t} = 0 \ \left(J=1, 2, 3, \ldots, N \right) \tag{66}$$

The freely drained boundary condition expressed by Equation (65) represents a scenario in

which water is permitted to flow unrestrictedly from the soil layer, typically describing a situation where the soil is in contact with a permeable layer or the atmosphere, thereby facilitating the unimpeded outflow of water from the soil. Conversely, the undrained condition described using Equation (66) at the bottom implies that water cannot escape from the soil layer, simulating a situation where the soil is underlain by an impermeable layer, such as bedrock or a dense clay layer, thereby preventing the outflow of water.

During the PVD-assisted soil flushing process, vacuum pressures are applied in the IPVWs and EPVWs. Under these conditions, the pressure boundary can be expressed as follows:

$$u_{eI,1}^{t} = u_{vac} \quad (I = 1, 2, ..., M) \tag{67}$$

where u_{vac} is the vacuum pressure value.

In addition, the interface between different soil layers, the smear and undisturbed zone interface satisfies the continuity condition. Assuming that the only difference between the smear zone and the undisturbed zone is the radial permeability coefficients. Then we can obtain:

$$k_{r_s^R} \frac{\partial u_{eI,r_s^R}^{t}}{\partial r} = k_{r_s^L} \frac{\partial u_{eI,r_s^L}^{t}}{\partial r} \quad (I = 0, 1, 2, 3, \ldots, M) \tag{68}$$

where the subscript R and L represent the right side and left side of the interface between the smear zone and undisturbed zone; the subscript s represents the smear zone; r_s is the radial element number at the smear zone boundary.

For the boundary conditions involving the solute, two primary types of bottom concentration boundary conditions are typically considered (Xie et al., 2016):

$$c^{t}_{M,J} = \text{constant}\ \left(J = 1, 2, ..., N\right) \tag{69}$$

$$c^{t}_{M,J} - c^{t}_{M-1,J} = 0\ \left(\ J=1,\ 2,\ 3,\ ...\ ,\ N\right) \tag{70}$$

Equations (69) and (70) represent the first-type Dirichlet boundary condition and the second-type Neumann boundary condition, respectively. The first-type boundary generally corresponds to a clay liner situated above a leakage detection layer or a permeable layer that facilitates the rapid removal of contaminants from the base of the system. The second type boundary represents an impermeable base stratum. This bottom boundary can be reasonably assumed to fully restrict contaminant transport.

The numerical solution of the coupled model can subsequently be derived by programming the aforementioned difference equations in MATLAB.

3 Model verification

3.1 Comparison with 1D consolidation and solute transport test

To validate the performance of the developed model, the coupled consolidation and solute transport tests J4 and J7, as reported by Lee et al. (2009), were employed. The experimental setup for tests is illustrated in Figure 4. The test consists of two distinct layers: a contaminated slurry layer and an uncontaminated slurry layer, both placed within the test cell. Initially, the heights of the contaminated and uncontaminated slurry layers in test J4 are 19 mm and 51.1 mm. The corresponding heights in J7 are 51.1 mm and 17.5 mm. The specimen has a diameter of 102 mm. The top boundary is permeable, allowing drainage, while all other boundaries are impermeable. All boundaries for solute transport are assigned zero gradient conditions

401 ($\partial c/\partial z = 0$ or $\partial c/\partial r = 0$). The modelling parameters, including the initial conditions of the
402 specimens, as well as the consolidation and solute transport parameters, are presented in Table
403 2. It should be noted that all the modelling parameters in Table 2 are obtained by element or
404 soil column tests. The effective diffusion coefficient D_e was calculated using the formula:
405 $D_e = D_0 n^M + \alpha_L v_w / n$, where D_0 is the free solution diffusion coefficient in water, M is the
406 effective diffusion coefficient exponent, α_L the longitudinal dispersity.

407 Figure 5 compares the experimental measurements with numerical solutions obtained
408 from CST2 (Lee and Fox, 2009) and the proposed model. Both methods capture the overall
409 consolidation and solute transport behavior with reasonable accuracy, and their predictions are
410 broadly consistent with the experimental data, with only slight deviations observed. Results
411 obtained by ignoring consolidation during solute transport are also included for comparison.
412 While both coupled and uncoupled predictions capture the general migration trends, neglecting
413 consolidation leads to significantly slower solute migration, lower effluent concentrations, and
414 underestimation of adsorbed solute amounts. These findings highlight the importance of
415 incorporating consolidation-induced hydro-mechanical effects in accurately modeling
416 contaminant migration in soft soils.

417 Table 2 Parameters in the modeling of consolidation-induced solute transport test (Lee et al., 2009)

Parameters	Methods	Values for J4	Values for J7	Unit
κ	Oedometer test	0.011	0.011	1
λ	Oedometer test	0.28	0.28	1
ψ	Oedometer test	-	-	1
t_0	Oedometer test	1	1	day
e_0	Oedometer test	2.52	2.51	1

σ_0' (kPa)	Oedometer test	0.8	0.8	kPa
σ_p' (kPa)	Oedometer test	0.8	0.8	kPa
e_p^{ep}	Oedometer test	2.52	2.51	1
Initial concentration of Br^-	Initial condition	1672	1697	mg/L
Initial concentration of K^+	Initial condition	259	295.8	mg/L
Diffusion coefficient D_0 of Br^-	Diffusion test	20.8×10^{-10}	20.8×10^{-10}	m^2/s
Diffusion coefficient D_0 of K^+	Diffusion test	19.6×10^{-10}	19.6×10^{-10}	m^2/s
Density of clay, ρ_d	Initial condition	2610	2610	kg/m^3
Sorption coefficient of K^+, K_d	Batch test	3×10^{-3}	3×10^{-3}	m^3/kg
Initial height of uncontaminated layer	Initial condition	52.1	17.5	mm
Initial height of contaminated layer	Initial condition	19	51.1	mm
M of Br^-	Dispersion test	1.82	1.82	1
M of K^+	Dispersion test	1.82	1.82	1
α_L of Br^-	Dispersion test	0	0	mm
α_L of K^+	Dispersion test	20	20	mm

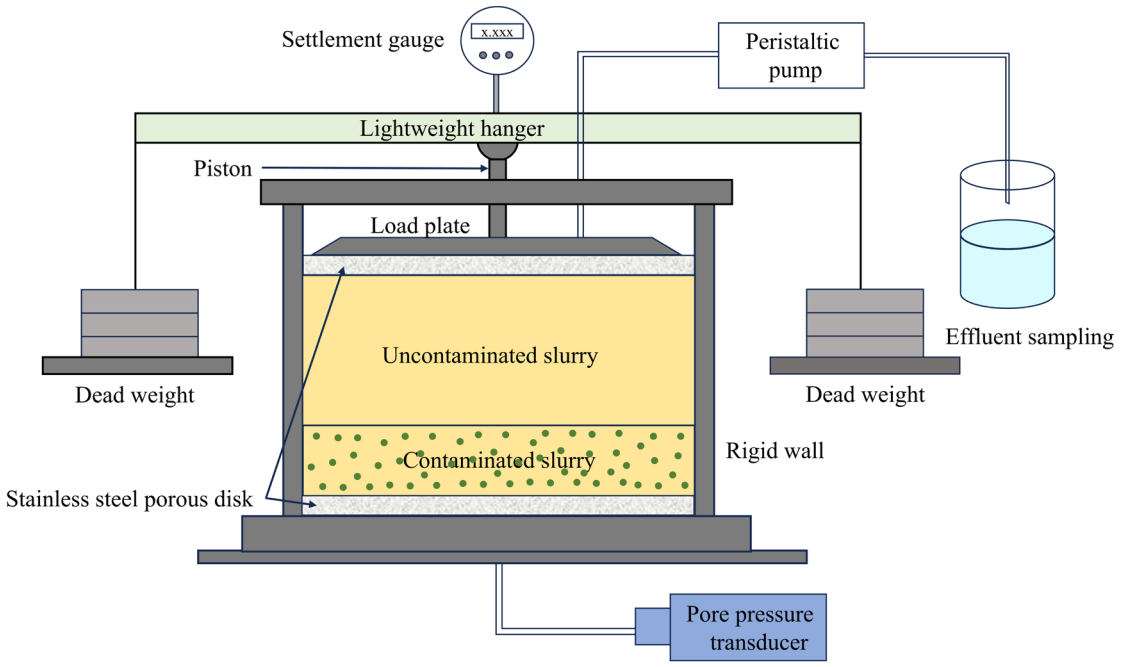

418

419 Figure 4 Schematic diagram of consolidation test apparatus (Lee et al., 2009)

420 []

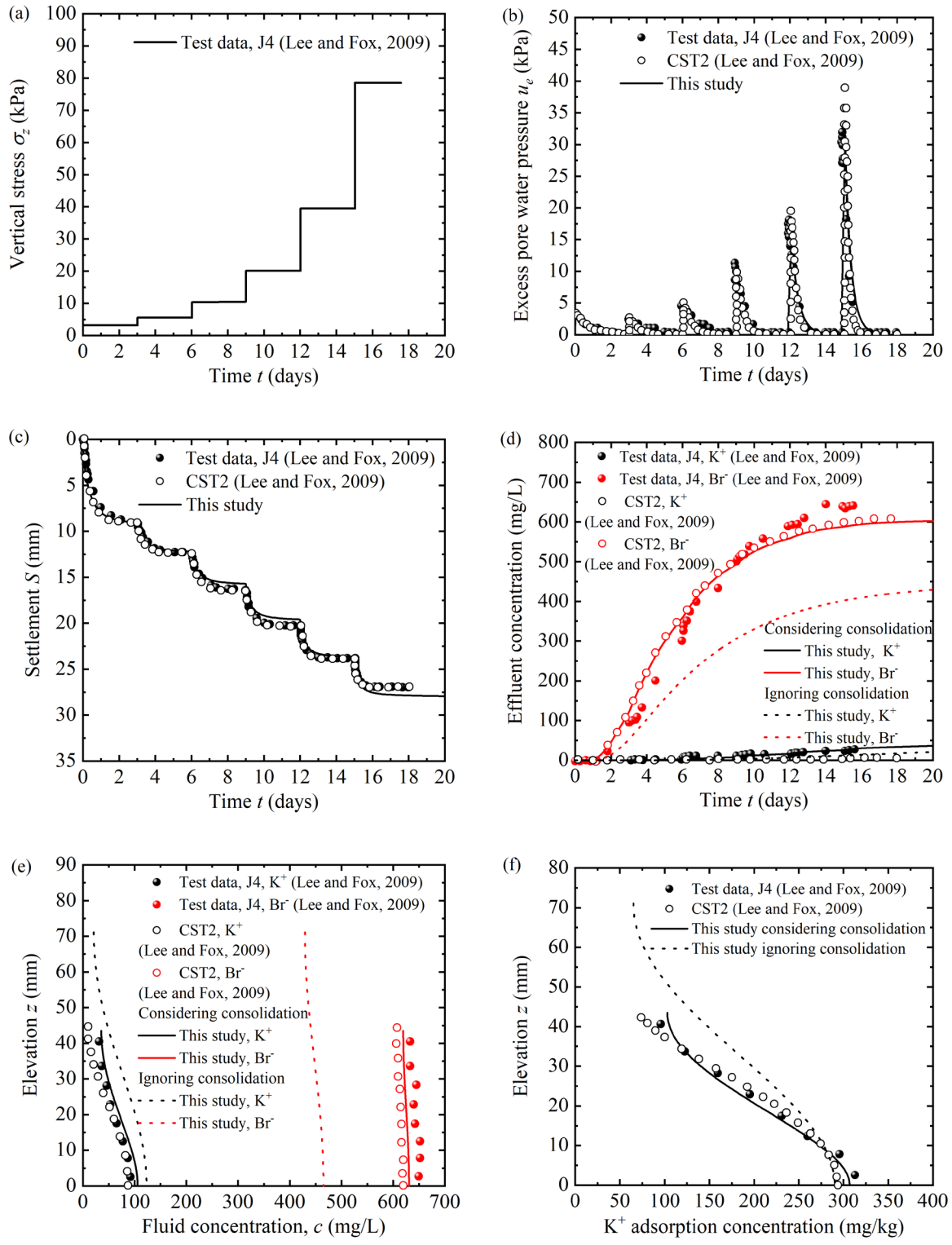

Figure 5 Comparisons of the modeling results and measured results (Test J4, Lee and Fox, 2009): (a) loading schedule; (b) excess pore water pressure; (c) soil surface settlement; (d) effluent K^+ and Br- concentrations; (e) fluid concentration distributions of K^+ and Br^-; and (f) Sorbed K^+ concentration

Figure 6 illustrates the results of Test J7 under complex loading conditions. Both CST2 and the proposed model reproduce the observed consolidation responses and solute transport behavior with reasonable accuracy. Minor discrepancies are noted between simulation results and experimental data in the fluid-phase and adsorbed solute concentrations, particularly under multi-stage loading, but overall agreement with measurements is maintained.

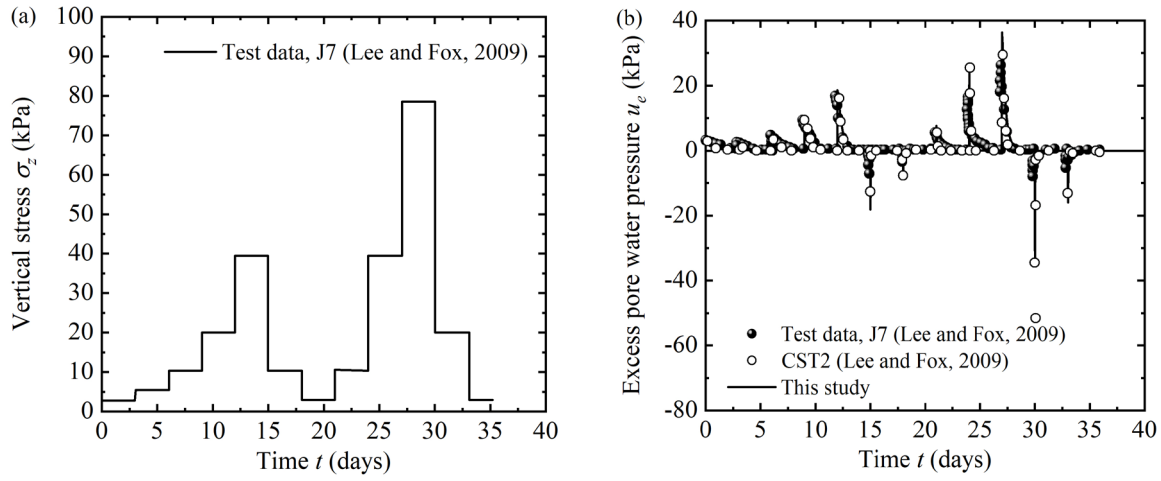

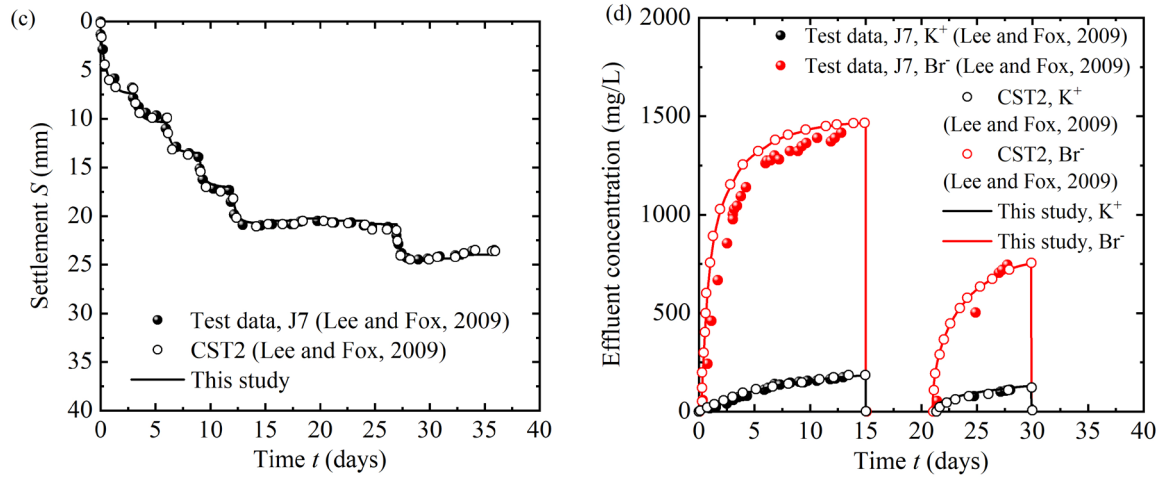

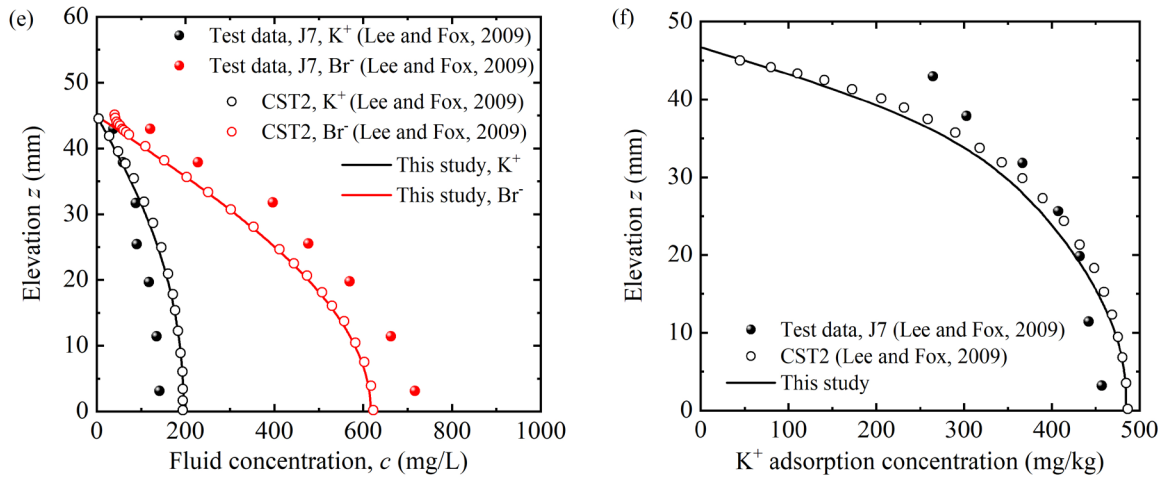

Figure 6 Comparisons of the modeling results and measured results (Test J7, Lee and Fox, 2009): (a) loading schedule; (b) excess pore water pressure; (c) soil surface settlement; (d) effluent K^+ and Br- concentrations; (e) fluid concentration distributions of K^+ and Br^-; and (f) Sorbed K^+ concentration

3.2 Comparison with existing analytical solution

Jiang et al. (2023) and Jiang et al. (2024) reported analytical solutions of the axisymmetric solute transport model for double-layered and multi-layered contaminated soils. The cases of soils with a single layer (Figure 4(a)) and three layers (Figure 8(a)) were selected to be simulated by the developed model of this study. It should be noted that the models of Jiang et al. (2023) and Jiang et al. (2024) ignored the consolidation effect. The vacuum pressures in the injection and extraction wells were simplified into injection/ extraction rates. Therefore, in these two cases, the developed model closed the consolidation equation. The initial and boundaries are the same as the models of Jiang et al. (2023) and Jiang et al. (2024). The parameters used in the simulations are listed in Table 3 and Table 4. The governing equation of the solute transport model proposed by Jiang et al. (2023) and Jiang et al. (2024) are as

follows:

$$R_{dj}\frac{\partial c_j}{\partial t}=\frac{1}{r}\frac{\partial}{\partial r}\left[D_{rj}r\frac{\partial c_j}{\partial r}\right]-\frac{1}{n_j r}\frac{\partial}{\partial r}\left[rq_{rj}c_j\right]+D_{vj}\frac{\partial^2 c_j}{\partial \xi^2} \tag{71}$$

where:

$$R_{dj}=1+\rho_{dj}K_{d_j}/n_j \tag{72}$$

$$q_{rj}=Q_{0j}/(2\pi Hr) \tag{73}$$

$$D_{vj}=D^*+\alpha_{vj}q_{vj}/n_j \tag{74}$$

$$D_{rj}=D^*+\alpha_{rj}q_{rj}/n_j=D^*+\alpha_{rj}Q_{0j}/\left(2\pi Hn_j r\right) \tag{75}$$

Figure 4 (b) and Figure 8(b) show the calculated solute concentration distributions along the radial direction of models of Jiang et al. (2023), Jiang et al. (2024), and this study. The solute distributions of single-layered and three-layered contaminated soils simulated by the developed model are consistent with the analytical solutions. This indicates that the developed model has the capacity to analyze the flushing process assisted by PVD with vacuum pressure.

Table 3 Parameters used in the modelling of contaminated soil with a single layer proposed by Jiang et al. (2023)

Parameters	Value	Unit
Initial void ratio, e_0	0.45	1
Unit weight, ρ_d	1909	kg/m^3
Extraction/injection rate, Q_0	0.26	m^3/h
Radial dispersivity, α_r	2	m
Vertical dispersivity, α_v	1	m
Sorption coefficient, K_d	0.00115	m^3/kg
Initial concentration of contaminated soil, c_0	100	mg/L

Table 4 Parameters used in the modelling of contaminated soil with three layers proposed by Jiang et al. (2024)

Parameters	Value			Unit
	Layer 1	Layer 2	Layer 3	
Initial void ratio, e_0	0.75	0.69	0.64	1
Unit weight, ρ_d	1550	1605	1659	kg/m^3
Effective diffusion coefficient, D^*	3.75×10^{-6}	3.75×10^{-6}	3.75×10^{-6}	m^2/h
Extraction/injection rate, Q_0	0.026	0.026	0.026	m^3/h
Radial dispersivity, α_r	2	2	2	m
Vertical dispersivity, α_z	1	1	1	m
Sorption coefficient, K_d	0	0	0	m^3/kg
Initial concentration of contaminated soil, c_0	95	86	78	mg/L
Decay constant of the initial concentration of the contaminated liquid along the depth, θ	0.1	0.1	0.1	m^{-1}

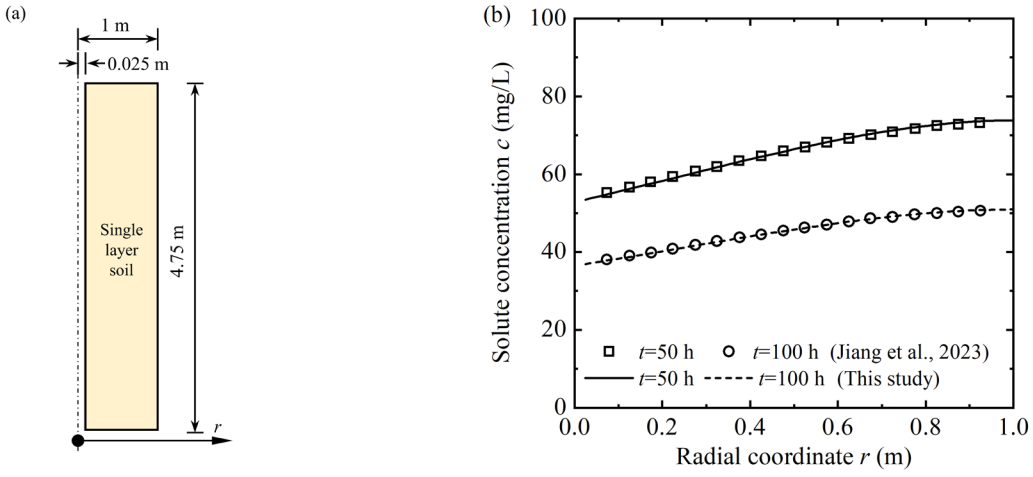

Figure 7 Comparison with analytical solution of contaminated soils with single layer (Jiang et al., 2023) : (a) schematic diagram of the model, and (b) solute concentration distribution

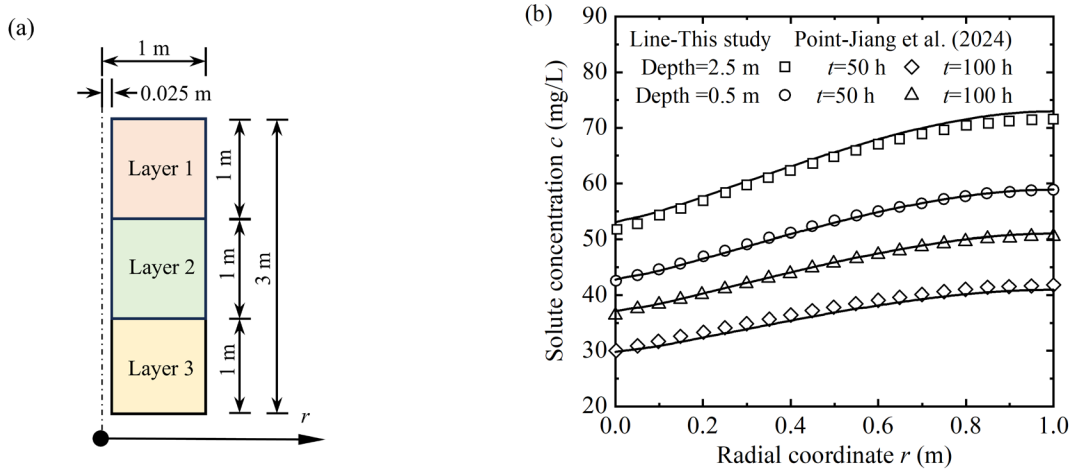

Figure 8 Comparison with analytical solution of contaminated soils with three layers (Jiang et al., 2024): (a) schematic diagram of the model, and (b) solute concentration distribution

3.3 Comparison with PVD-enhanced flushing tests

Park and Shin (2009) conducted the PVD-enhanced flushing model tests on contaminated soils under both dense and loose conditions, with the PVD layout illustrated in Figure 9. The developed model was subsequently applied to simulate this case. The model parameters as shown in Table 5 used in the simulation were derived from the data provided by Park and Shin (2009). A comparison of the predicted and measured results, as shown in Figure 10, demonstrates that the developed model accurately captures the changes in tracer (KBr) concentration over time under both dense and loose conditions. To distinguish between loose and dense soil conditions in the simulations presented in Figure 10, different values of solid dry density (ρ_s) were employed, specifically 1442 kg/m³ for loose soil and 1638 kg/m³ for dense soil, respectively. These values are directly adopted from the reference study by Park and Shin (2009) and are summarized in Table 5. Solid density governs the adsorption term in the solute

485 transport equation, as it reflects the mass of solid matrix available for contaminant sorption.
486 Higher density corresponds to greater sorption capacity, which slows contaminant migration,
487 highlighting the role of compaction in solute transport behavior.

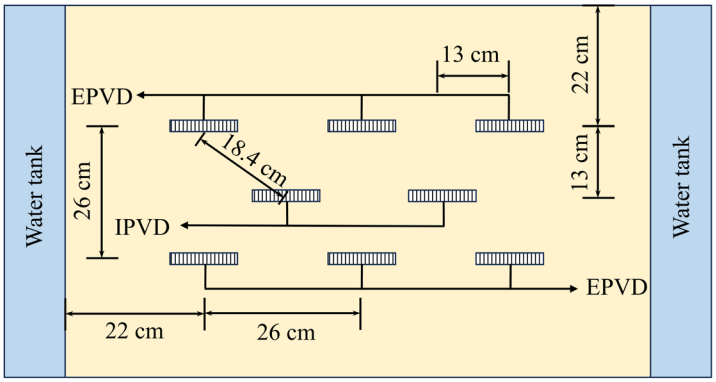

488

489 Figure 9 Plan view of PVD layout in the model test tank after Park and Shin (2009)

490 Table 5 Parameters in the modeling of contaminated soil reported by Park and Shin (2009)

Parameters	Value	Unit
Initial void ratio, e_0	0.25	1
Dry weight, ρ_d (dense condition)	1638	kg/m^3
Dry weight, ρ_d (loose condition)	1442	kg/m^3
Extraction/injection rate, Q_0	1.29×10^{-3}	m^3/h
Sorption coefficient, K_d	0	m^3/kg
Vertical flow velocity, q_z	2.5×10^{-3}	m/h
Radius inside the equivalent extraction drain well, r_e	0.18	m
The effective radius of the injection well, r_w	0.0065	m
Initial concentration of contaminated soil, c_0	100	mg/L

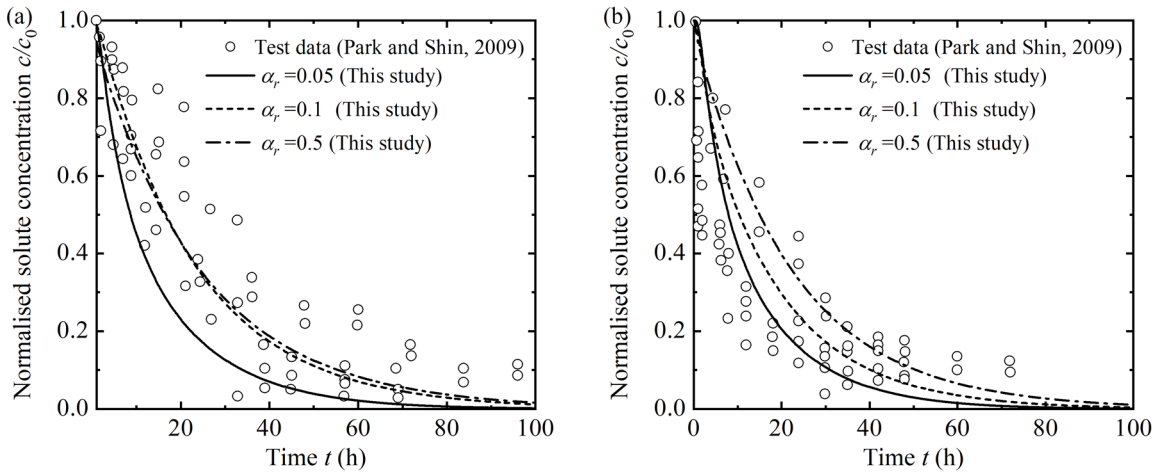

491

492 Figure 10 Comparison with calculated results and measured results (Park and Shin, 2009): (a) dense

493 condition; and (b) loose condition

494 In addition to the study by Park and Shin (2009), the bench-scale test conducted by Gabr

495 et al. (1996a) was replicated for comparison. In the aforementioned simulations, the vacuum

496 loads in the PVDs as injection and extraction wells were simplified into flow rates to model

497 the PVD-enhanced soil flushing. Although widely adopted by current models(Gabr et al.,

498 1996b; Park and Shin, 2009; Jiang et al., 2023; Jiang et al., 2024), this simplification deviates

499 from field conditions. In practical applications, vacuum is typically applied directly, rendering

500 the associated flow rates difficult to control. This discrepancy may result in an inaccurate

501 evaluation of effectiveness of PVD in accelerating the leaching of contaminated soil. The

502 proposed model, which incorporates excess pore water pressure, void ratio, and solute

503 concentration as variables, addresses this limitation. Figure 11(a) illustrates the configuration

504 of the injection and extraction wells. The pressures in the injection and extraction wells were

505 set at 13.8 kPa and -9.8 kPa, as established in the experiment by Gabr et al. (1996a). All

506 simulation parameters, except the effective diffusion coefficient listed in Table 6, were sourced

from Gabr et al. (1996a). The effective diffusion coefficients were determined through back-analysis.

Figure 11(b) presents a comparison between the predicted and measured results. The calculated results, obtained using three different diffusion coefficients in the proposed model, effectively encompass the range of solute concentrations. This highlights the advantage of the proposed model in directly incorporating realistic boundary conditions rather than relying on artificial assumptions commonly used in simplified approaches. Compared with existing simplified approaches, the proposed model allows direct incorporation of pore pressure boundary conditions measured in the field during PVD-assisted flushing, eliminating the need for assumed or artificially prescribed boundary values. This feature enhances the physical realism of the simulations and improves the applicability of the model in engineering practice, where such boundary conditions can be directly obtained from monitoring data. It is noted that the above soil-flushing experiments were designed to focus on solute transport and flushing efficiency, without monitoring consolidation-related variables such as settlement or pore pressure dissipation. Therefore, direct validation of the model outputs for consolidation variables was not possible.

Table 6 Parameters used in the modelling of test reported by Gabr et al. (1996a)

Parameters	Value	Unit
Initial void ratio, e_0	0.33	1
Sorption coefficient, K_d	1×10^{-4}	m^3/kg
Permeability coefficient, k	5×10^{-4}	cm/s
Radius inside the equivalent extraction drain well, r_e	0.14	m
The effective radius of the injection well, r_w	0.011	m

Initial concentration of contaminated soil, c_0	100	mg/L

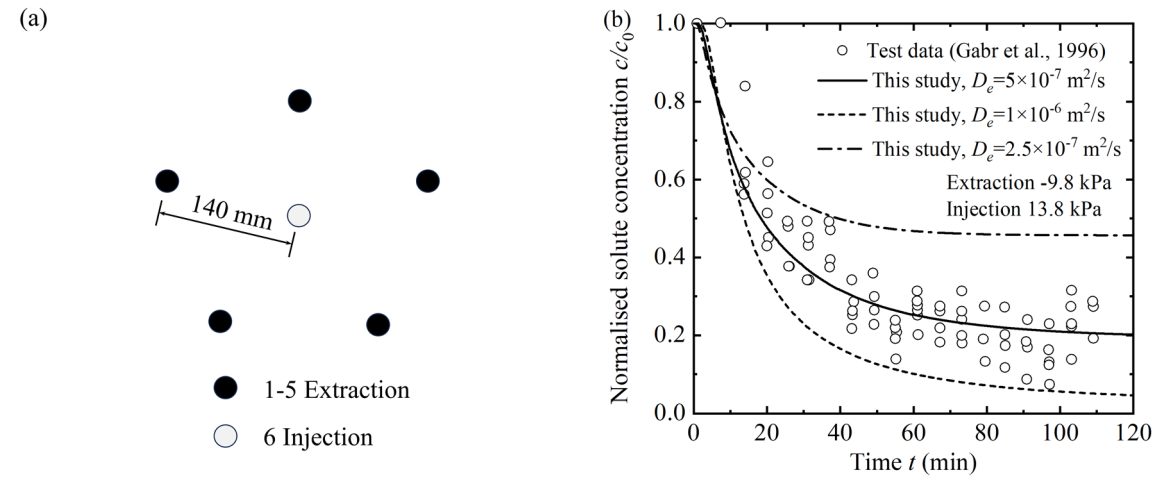

Figure 11 Comparison between calculated results and measured results (Gabr et al., 1996a): (a) plan view of PVD layout, and (b) solute concentration evolution

3.4 Comparison with finite element (FE) solution from COMSOL software

To independently verify the correctness and reliability of the proposed solution, a benchmark comparison was conducted using COMSOL Multiphysics, a widely recognized multiphysics finite element (FE) software. The COMSOL PDE module was selected because it enables the direct implementation of the coupled consolidation–solute transport governing equations developed in this study, thereby providing a rigorous FE benchmark under identical conditions. Moreover, as existing literature contains very few studies addressing the fully coupled axisymmetric large-strain consolidation and solute transport problem, no widely accepted benchmark solutions are available, making a direct comparison with a commercial FE solver particularly valuable. The benchmark case was designed as a simplified axisymmetric unit cell model representing a PVD-improved ground. The soil layer height was

set to 3 m, with the PVD embedded through the full depth. The equivalent drain radius was r_w=0.01 m, and the influence zone radius was r_e=0.5 m. To isolate the effects of vacuum-assisted consolidation and solute transport, smear zone effects and adsorption were omitted. All relevant material parameters and initial conditions are listed in Table 7, and identical values were applied in both the FD and FE models to ensure a fair comparison.

Table 7 Parameters in the comparison with FE solution

Parameters	value	Unit
κ	0.025	1
λ	0.065	1
ψ	0.003	1
t_0	1	day
e_0	0.25	1
σ'_0 (kPa)	78	kPa
σ'_p (kPa)	78	kPa
e_p^{ep}	0.25	1
Vertical permeability coefficient k_v Radial permeability coefficient k_r	5×10^{-9}	m/s
Vertical effective diffusion coefficient D_{ev} Radial effective diffusion coefficient D_{er}	2.5×10^{-8}	m^2/s
Density of clay, ρ_d	2000	kg/m^3
Sorption coefficient of K^+, K_d	0	L/kg

Figure 12 compares the solute concentration and excess pore water pressure profiles under vacuum pressures of –40 kPa and –20 kPa, obtained from the proposed solution and the FE solution from the COMSOL PDE module. As shown in Figure 12, the proposed solution in this study closely matches the FE solution for both solute concentration and excess pore water pressure profiles across the radial domain. Both solutions capture the temporal evolution of

solute migration toward the drain and the dissipation of excess pore pressure during consolidation. This strong consistency validates the correctness and robustness of the proposed coupled consolidation–solute transport model and indicates that the present numerical solution can serve as a computationally efficient yet reliable alternative to commercial FE solvers for engineering applications.

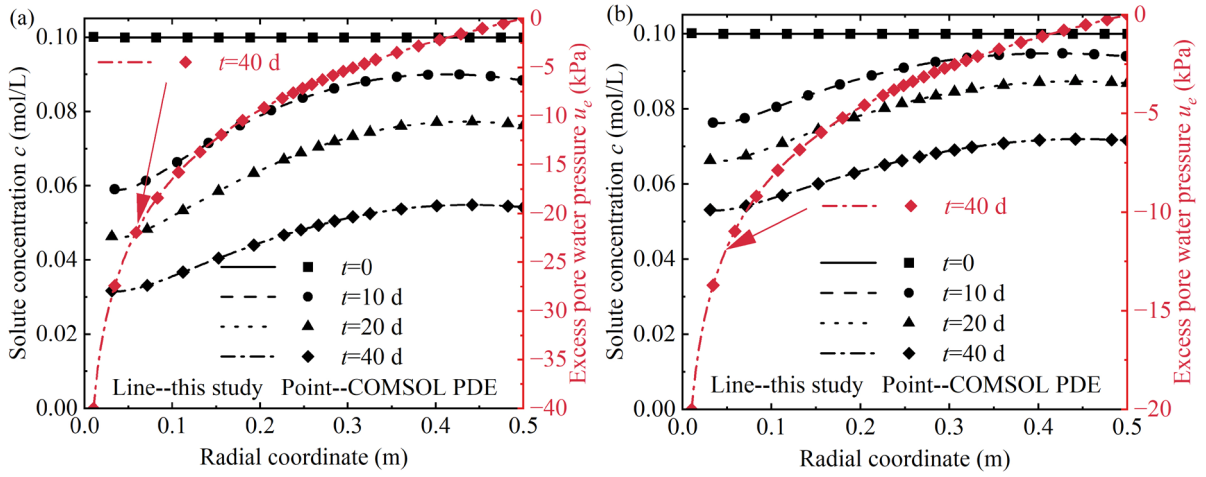

Figure 12 Comparison of solute concentration and excess pore water pressure simulated by the proposed solution and the COMSOL PDE module under different vacuum pressures in IPVW: (a) −40 kPa; (b) −20 kPa

4 Parameter analysis of engineering design concerns

Building upon the proposed axisymmetric mathematical model that couples consolidation and solute transport, parametric studies were conducted to systematically investigate several key factors influencing soil flushing efficiency in engineering applications. These factors include vacuum pressure in PVD, PVD spacing, and the penetration length of PVD. In this analysis, the height of a single contaminated soil layer is assumed to be 3 meters, with a uniform

solute concentration of 0.1 mol/L. The parameters used in this part are displayed in Table 7. To assess the efficiency, a cleanup efficiency index, termed was called vacuum-normalized concentration removal rate and and denoted as φ, is defined as the reduction rate of solute concentration per unit vacuum pressure:

$$\varphi = 100\left(c_0 - c\right) / c_0 / u_{vac} \tag{76}$$

4.1 Vacuum pressure in PVDs

Figure 13 to Figure 15 show the evolution of the solute concentration distribution under varying vacuum pressures of -10 kPa, -20 kPa, and -40 kPa. The results reveal that the solute concentration gradient diminishes over time, demonstrating the effectiveness of the PVD-assisted flushing method in solute removal. Higher vacuum pressure has a more pronounced decrease in the whole zone, particularly the zone close to the PVD.

Figure 16 summarizes the cleanup efficiency defined by Equation (76). Figure 16(a) depicts the solute concentration at various radial positions (r=0.1 m, 0.25m, 0.25m), demonstrating that higher vacuum pressures lead to faster and more significant reductions in solute concentration. Figure 14(b) highlights the overall cleanup efficiency, showing a clear positive correlation between vacuum pressure and the rate of efficiency improvement. In conclusion, increasing vacuum pressure enhances solute migration and cleanup efficiency, especially in the early stages, making it a critical parameter for optimizing remediation processes.

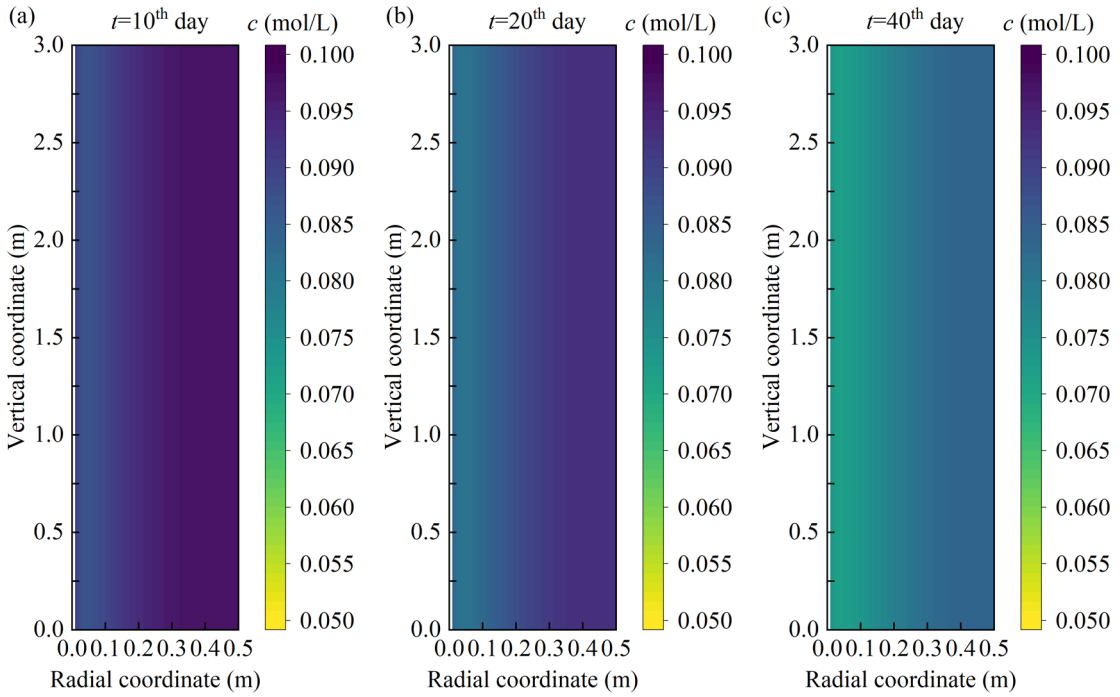

585

586 Figure 13 Solute distribution evolution under a vacuum pressure of -10 kPa and a PVD spacing of 0.5 m:

587 (a) t=10th day, (b) t=20th day, and (c) t=40th day

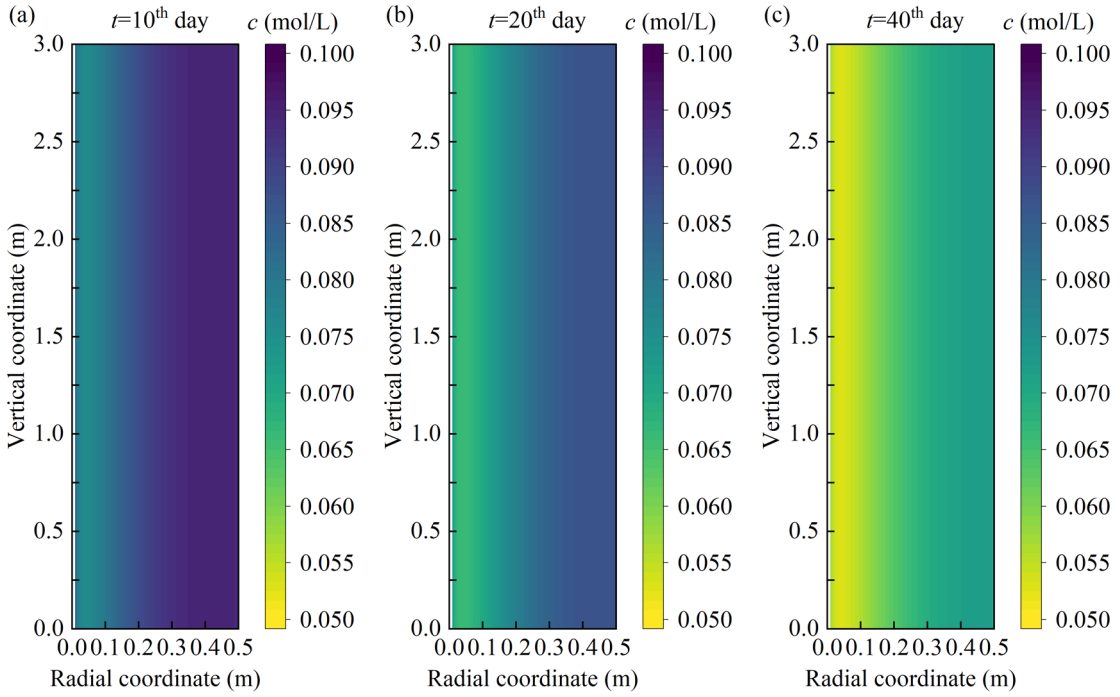

588

589 Figure 14 Solute distribution evolution under a vacuum pressure of -20 kPa and a PVD spacing of 0.5 m:

590 (a) t=10th day, (b) t=20th day, and (c) t=40th day

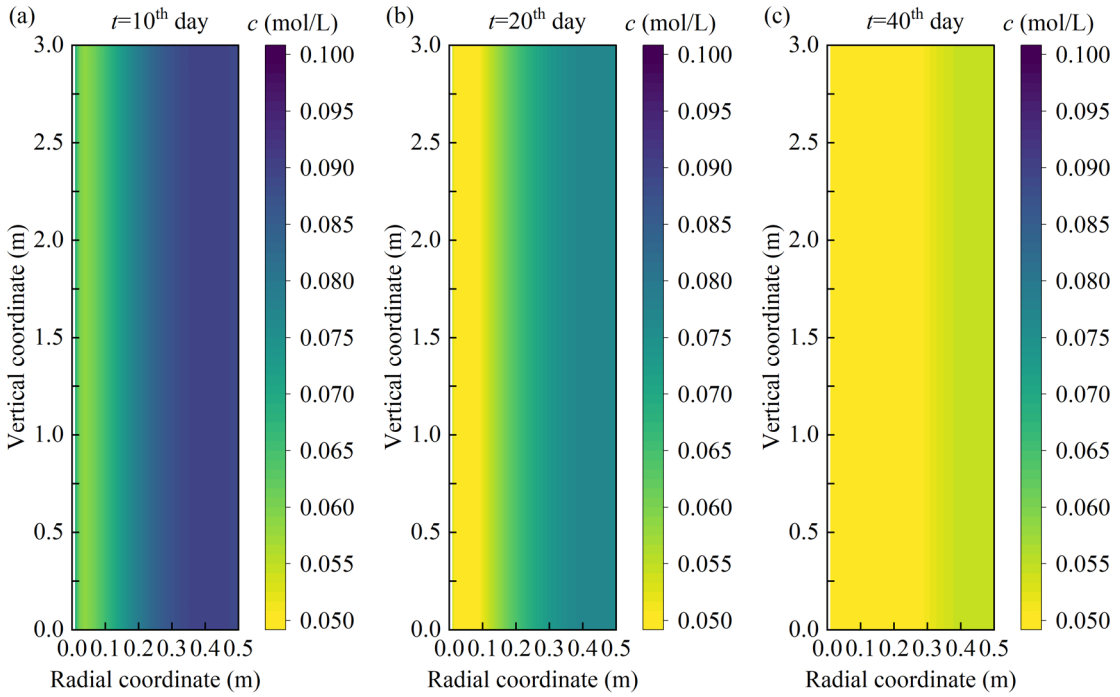

Figure 15 Solute distribution evolution under a vacuum pressure of -40 kPa and a PVD spacing of 0.5 m: (a) t=10th day, (b) t=20th day, and (c) t=40th day

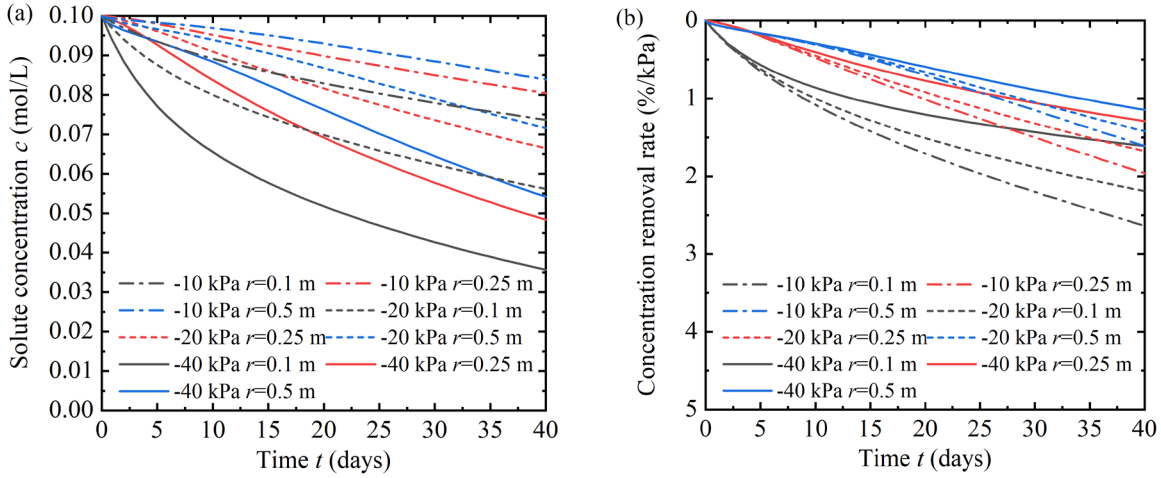

Figure 16 Clean-up effect of different positions under different vacuum pressures: (a) solute concentration, and (b) vacuum-normalized concentration removal rate

4.2 Spacing between PVDs

Figure 17 to Figure 19 present the evolution of the solute concentration distribution at

different time intervals under different PVD spacings of R=0.4 m, 0.5 m, and 0.6 m. From Figure 17 to Figure 19, it is clear that solute removal occurs more rapidly with smaller PVD spacings. By the 40th day, solute removal was nearly complete at a distance of 0.4 m from the PVD in the case of a 0.4 m spacing, whereas residual solute remained in other cases. Figure 20 presents a comparative analysis of solute concentration and clean-up efficiency at different radial distances. Figure 20(a) demonstrates a sharper drop in solute concentration along the radial direction with the spacing decreasing. Figure 20(b) further confirms that clean-up efficiency is highest when the PVD spacing is smallest. This suggests that decreasing PVD spacing is an effective strategy for enhancing the flushing of contaminated soils.

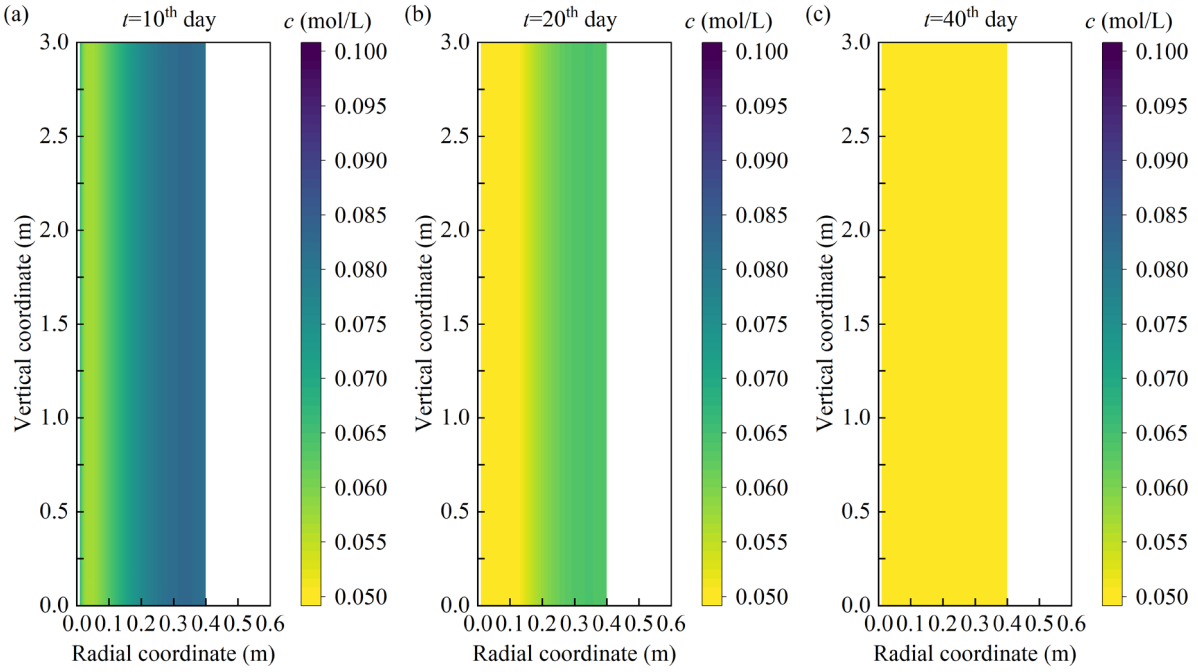

Figure 17 Solute distribution evolution under a vacuum pressure of -40 kPa and and a PVD spacing of 0.4 m: (a) t=10th day, (b) t=20th day, and (c) t=40th day

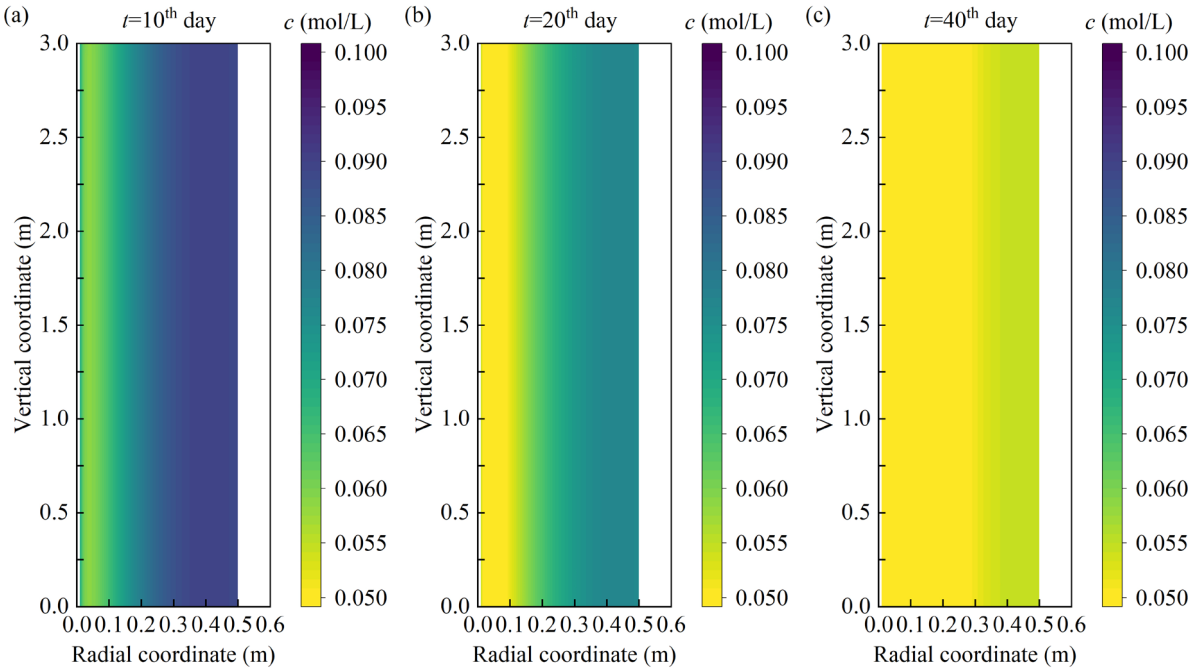

613

614 Figure 18 Solute distribution evolution under a vacuum pressure of -40 kPa and and a PVD spacing of 0.5

615 m: (a) t=10th day, (b) t=20th day, and (c) t=40th day

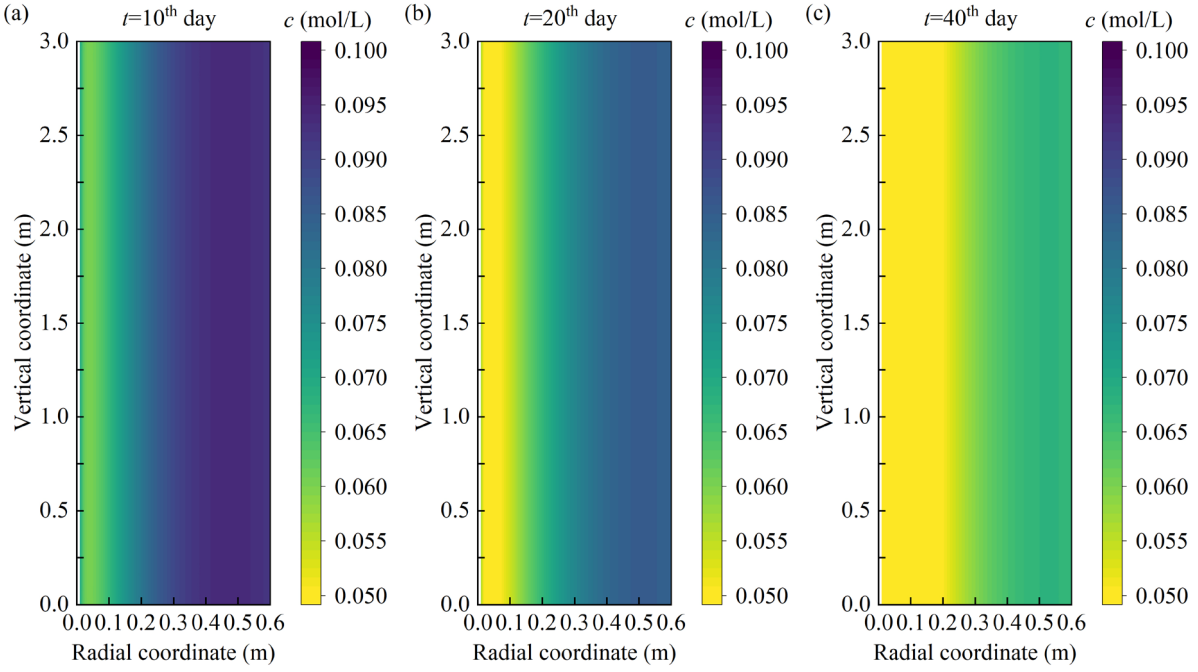

616

617 Figure 19 Solute distribution evolution under a vacuum pressure of -40 kPa and and a PVD spacing of 0.6

618 m: (a) t=10th day, (b) t=20th day, and (c) t=40th day

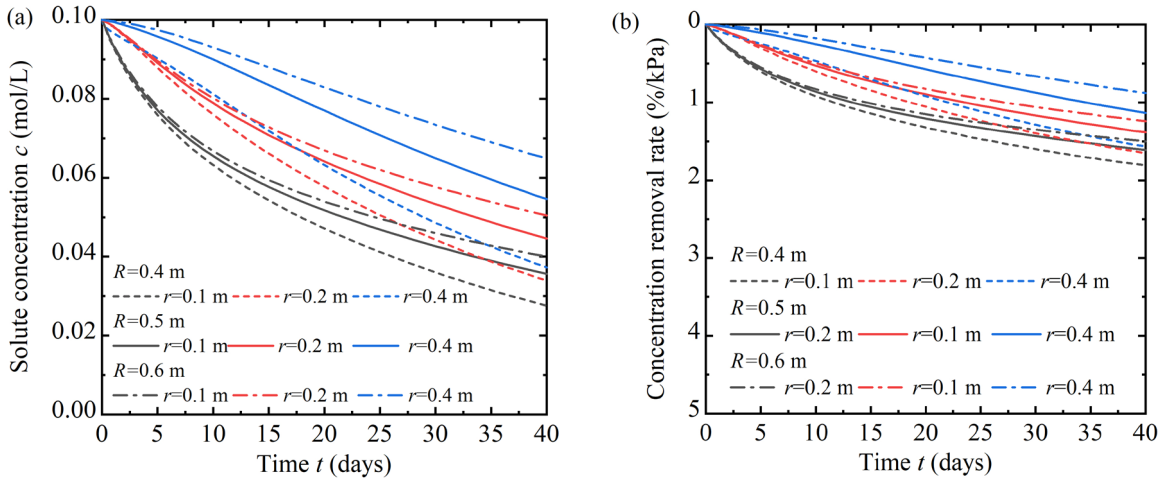

Figure 20 Clean-up effect of different positions under different PVD spacings: (a) solute concentration, and (b) vacuum-normalized concentration removal rate

4.3 Interaction between vacuum pressure and PVD spacing

Figure 21 compares the evolution of solute concentration at different radial distances for PVD spacings of 0.5 m and 0.4 m under vacuum pressures of -10 kPa and -40 kPa. At the fixed vacuum pressure, reducing the spacing accelerates solute concentration reduction at all radial positions, with the largest improvement observed near the drain (r=0.1 m). The benefit decreases with increasing radial distance, consistent with the attenuation of the vacuum-induced pore pressure gradient in the far field. This spacing advantage is more significant under -40 kPa than under -10 kPa, particularly during the early stages and in the near-drain region, indicating that a higher vacuum pressure amplifies the benefit of spacing reduction by strengthening pore pressure gradients and promoting more rapid advective–dispersive transport.

Conversely, at a fixed spacing, increasing vacuum pressure enhances the effectiveness of a given PVD spacing in accelerating solute removal, with the effect being more pronounced at

smaller spacing. For example, at r=0.1 m, the removal efficiency improvement from -10 kPa to -40 kPa is substantially greater when the spacing is 0.4 m than when it is 0.5 m, showing that closely spaced drains can better utilise the additional pore pressure gradient generated by higher vacuum levels. Overall, these findings demonstrate a clear synergistic interaction: higher vacuum pressure amplifies the performance gains from reduced spacing, especially in the near-drain region during the early stages of flushing.

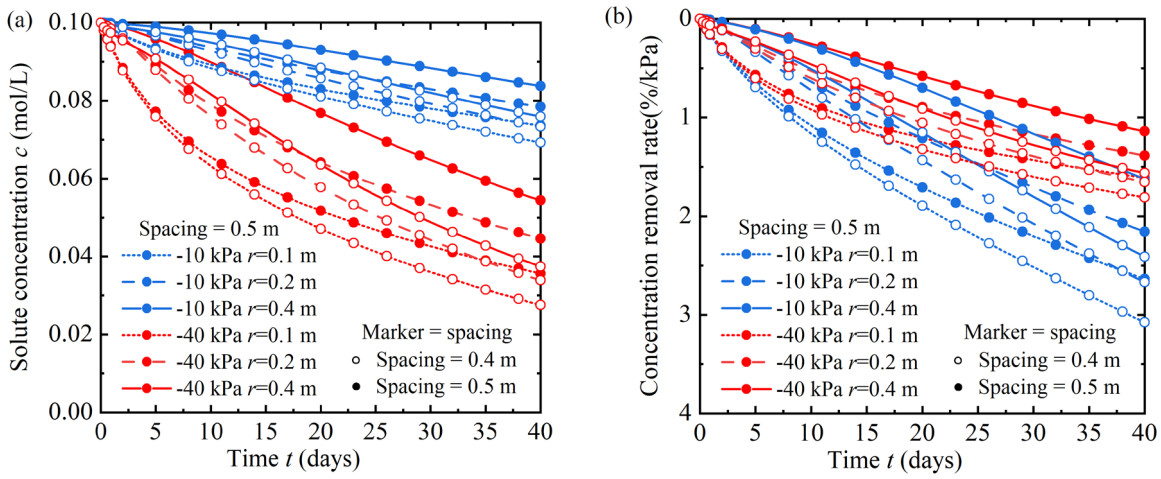

Figure 21 Interaction between PVD spacing and vacuum pressure on the clean-up effect of different positions: (a) solute concentration, and (b) vacuum-normalized concentration removal rate

4.4 Penetration length of PVDs

Figure 22 to Figure 24 illustrate the temporal variations of solute concentration distributions within the treated zone under different vacuum pressures and PVD spacings. The primary objective is to assess whether higher vacuum pressures or reduced PVD spacings can effectively extend the treated length of the soil flushing system. In this case, the PVD penetration length remains constant at 2 meters. The results presented in Figure 14 and Figure

22, which differ only in PVD penetration depths (3 m in Figure 14, 2 m in Figure 22), indicate that the radial extent of treatment remains almost unchanged despite variations in penetration depth. The treated depth does not increase over time unless the PVD penetration depth reaches the bottom of the treated soil layer. This phenomenon cannot be significantly improved merely by increasing the vacuum pressure in PVD, as evidenced by the results in Figure 23. Likewise, the comparison between Figure 17 and Figure 24 demonstrates that reducing PVD spacing did not significantly influence the treated depth. In conclusion, increasing vacuum pressure and reducing PVD spacing enhance solute removal along the radial direction, with greater vacuum pressures and narrower PVD spacings leading to more rapid and uniform remediation. However, these factors exhibit minimal influence on the treated depth of the soil flushing system when the PVD penetration length is less than the depth of the contaminated soil layer. This underscores the necessity of accurately characterizing the spatial distribution of pollutants during site remediation.

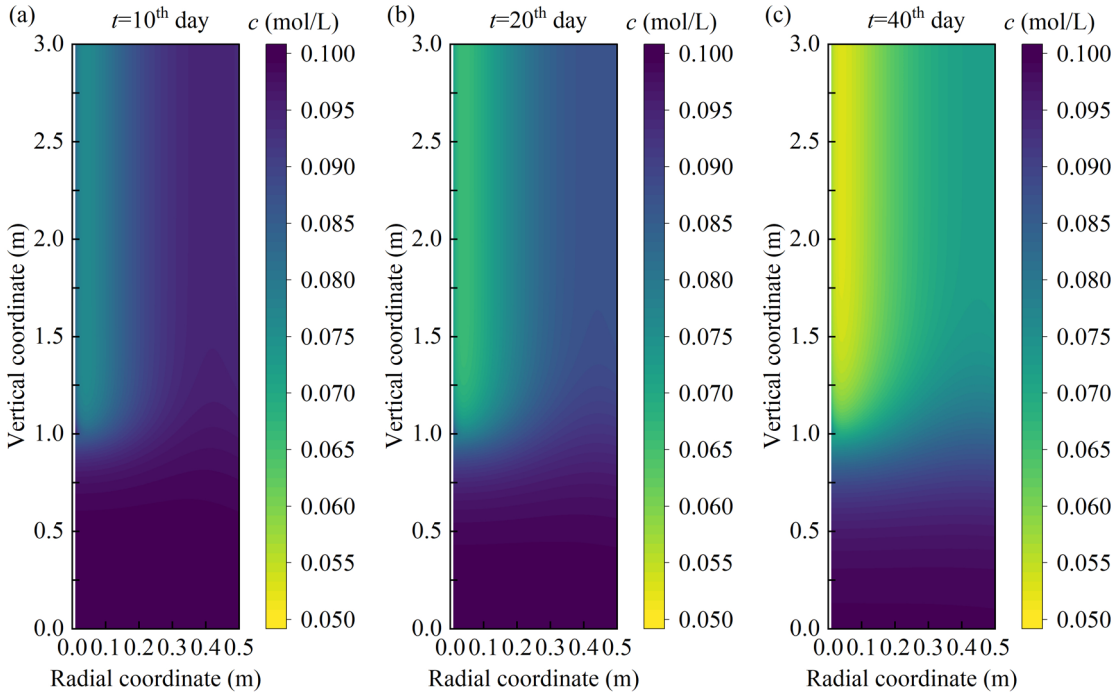

Figure 22 Solute distribution under a vacuum pressure of -20 kPa and a PVD spacing of 0.5 m: (a) t=10th day, (b) t=20th day, and (c) t=40th day

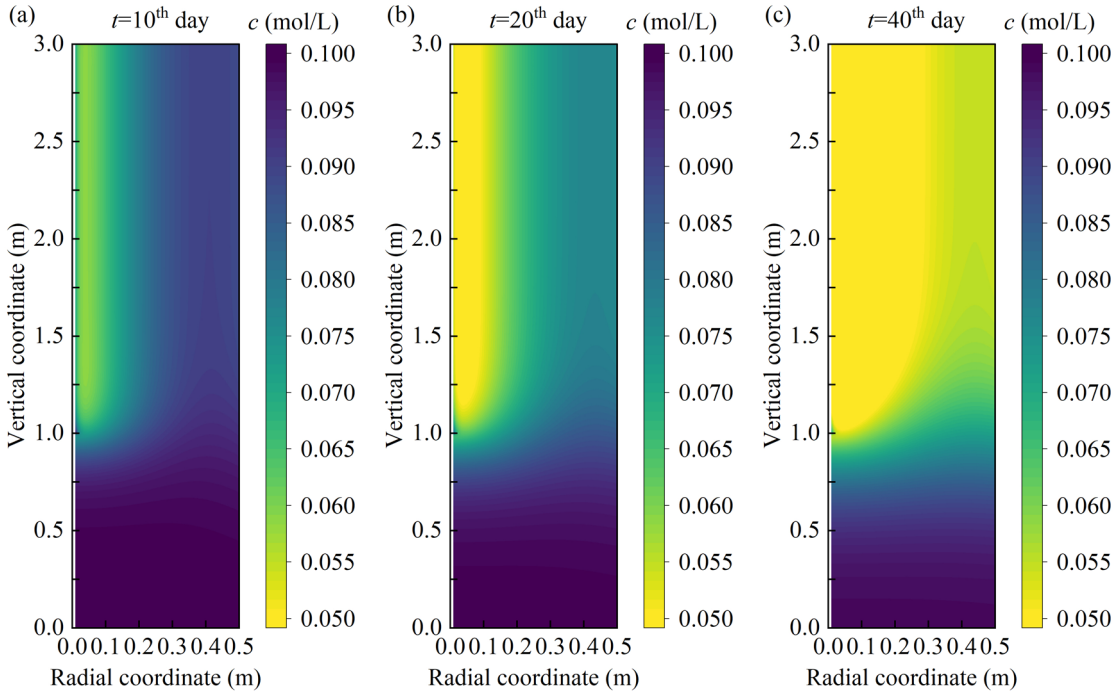

Figure 23 Solute distribution under a vacuum pressure of -40 kPa and a PVD spacing of 0.5 m: (a) t=10th day, (b) t=20th day, and (c) t=40th day

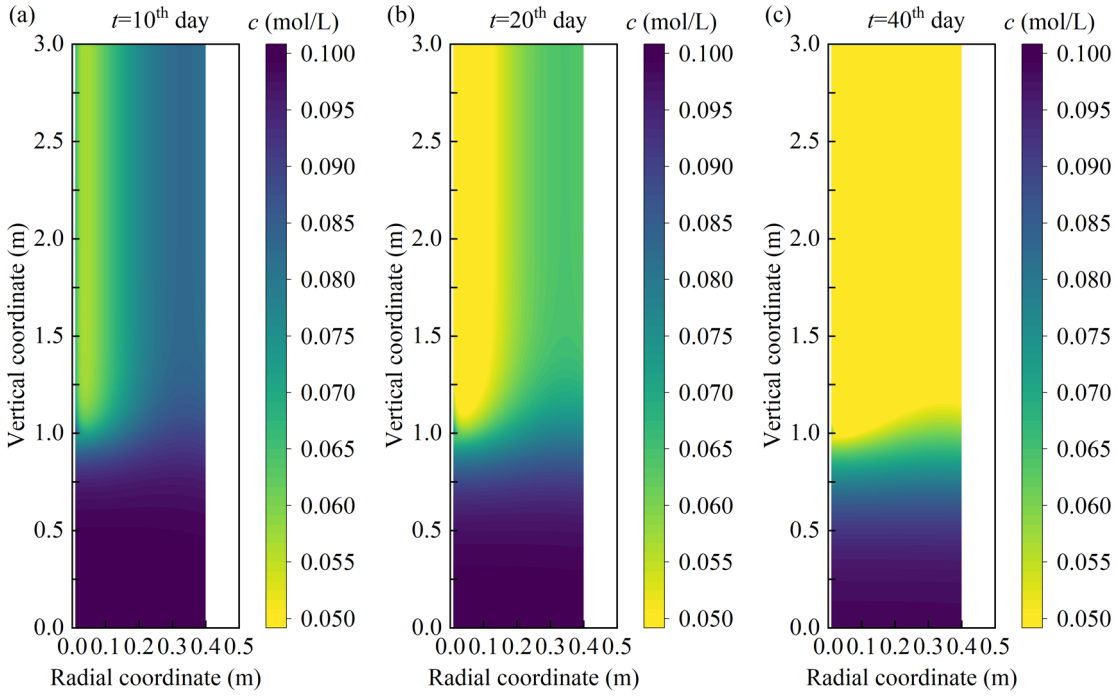

Figure 24 Solute distribution under a vacuum pressure of -40 kPa and a PVD spacing of 0.4 m: (a) t=10th day, (b) t=20th day, and (c) t=40th day

5 Effects of additional influencing factors

In addition to the specific parameter analysis of engineering design concerns, other key factors such as smear zone effect and adsorption effect are then discussed. In this part, except for the parameters related to smear zone and adsorption effect, the geometric and other simulation parameters remain the same as those in the parameter analysis part.

5.1 Smear zone effect

To account for the smear zone effect, the permeability coefficients of the smear zone and the undisturbed zone are differentiated. The smear zone, typically characterized by soil disturbance due to installation of vertical drains, is represented by a reduced permeability relative to the undisturbed soil, quantified using the permeability reduction ratio, expressed as:

$$\alpha = \frac{k_s}{k} \tag{77}$$

where k_s and k are the permeability coefficients of the smear zone and undisturbed zone, respectively. By assigning different α values, the model can systematically evaluate the effects of both permeability reduction and smear zone extent on consolidation and solute transport. This explicit treatment provides a more realistic prediction of installation-induced soil disturbance effects.

To quantify this influence of smear zone, a supplementary parameter analysis has been

conducted. The geometric and simulation parameters remain the same as those in the parameter analysis part. The smear zone radius is 0.1 m. The results, presented in Figures 25-27, show the temporal evolution of contaminant concentration profiles at 10, 20, and 40 days for varying permeability reduction ratios (α=1.0, 0.5, 0.2). The results indicate that the smear zone significantly impacts the effectiveness of flushing remediation. When α=1.0 (negligible disturbance), radial solute transport is rapid, enabling efficient flushing and significant contaminant reduction. As α decreases (0.5 and especially 0.2), the reduced permeability in the smear zone substantially hinders radial migration, slowing remediation and leaving higher residual concentrations over the same period. These results highlight not only the necessity of accurately characterizing smear zones but also their critical influence on the optimal design and expected performance of vertical drain–enhanced flushing systems.

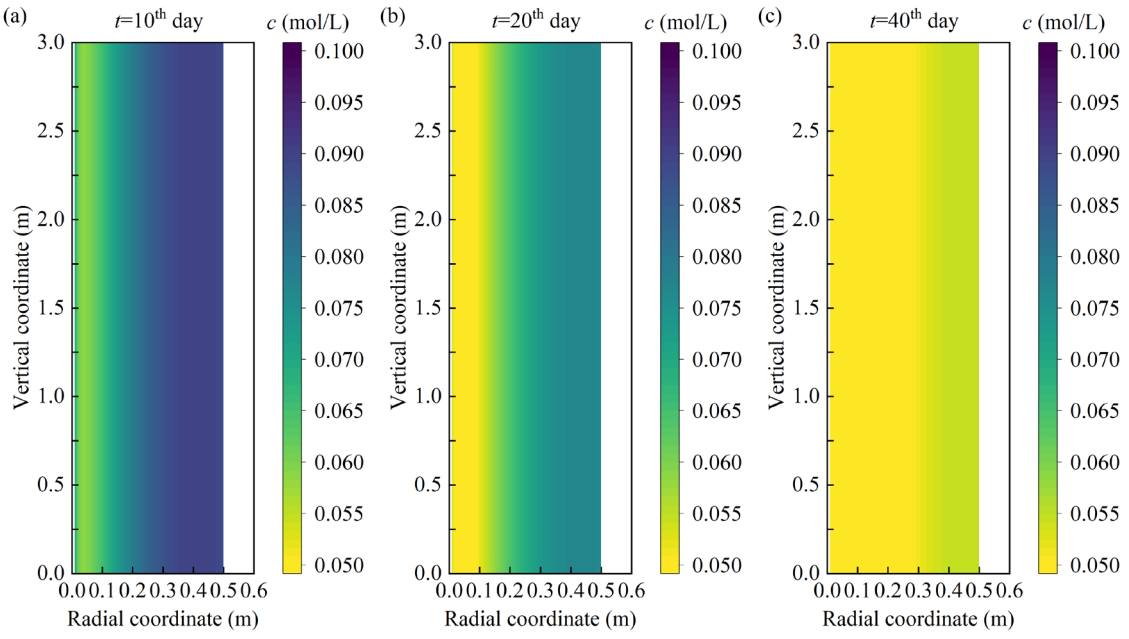

Figure 25 Solute distribution with a permeability reduction ratio α=1 in smear zone on solute distribution: (a) t=10th day, (b) t=20th day, and (c) t=40th day

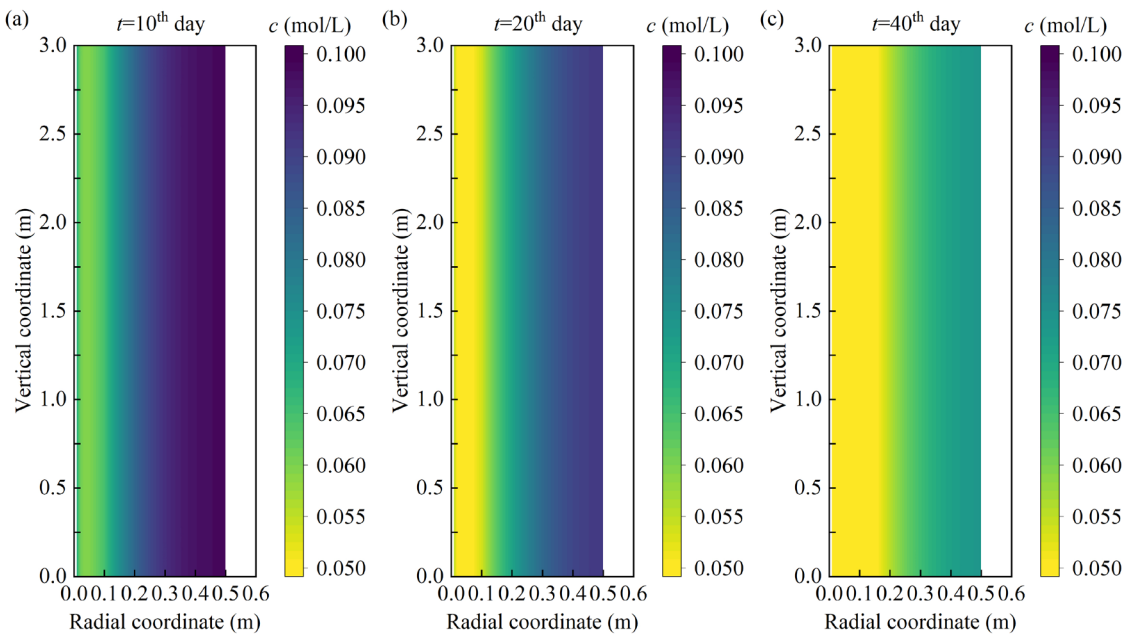

Figure 26 Solute distribution with a permeability reduction ratio α=0.5 in smear zone on solute distribution: (a) t=10th day, (b) t=20th day, and (c) t=40th day

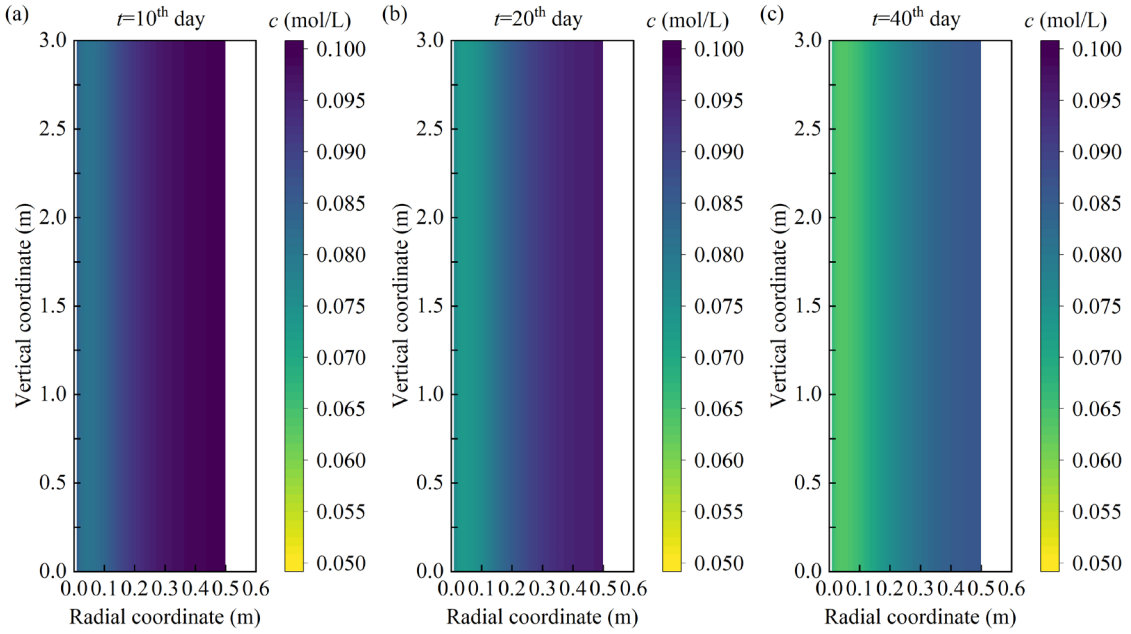

Figure 27 Solute distribution with a permeability reduction ratio α=0.2 in smear zone on solute distribution: (a) t=10th day, (b) t=20th day, and (c) t=40th day

5.2 Adsorption effect

Figures 28 to 30 illustrate the evolution of solute concentration distribution at different time intervals under adsorption coefficients K_d=0, 0.2 L/kg, and 0.4 L/kg, respectively. From these figures, it is evident that higher adsorption coefficients slow down solute migration. By the 40th day, a larger amount of residual solute remains in the soil matrix when K_d=0.4 L/kg, whereas a more pronounced reduction in solute concentration is observed for K_d=0. Figure 31 presents a comparative analysis of solute concentration and clean-up efficiency at different radial distances. Figure 31(a) shows that the decrease in solute concentration is more gradual with increasing adsorption coefficient, while Figure 31(b) confirms that clean-up efficiency decreases as K_d increases. These findings confirm that adsorption significantly impedes contaminant removal, underscoring the necessity of accounting for adsorption effects in the design and optimization of flushing-based soil remediation.

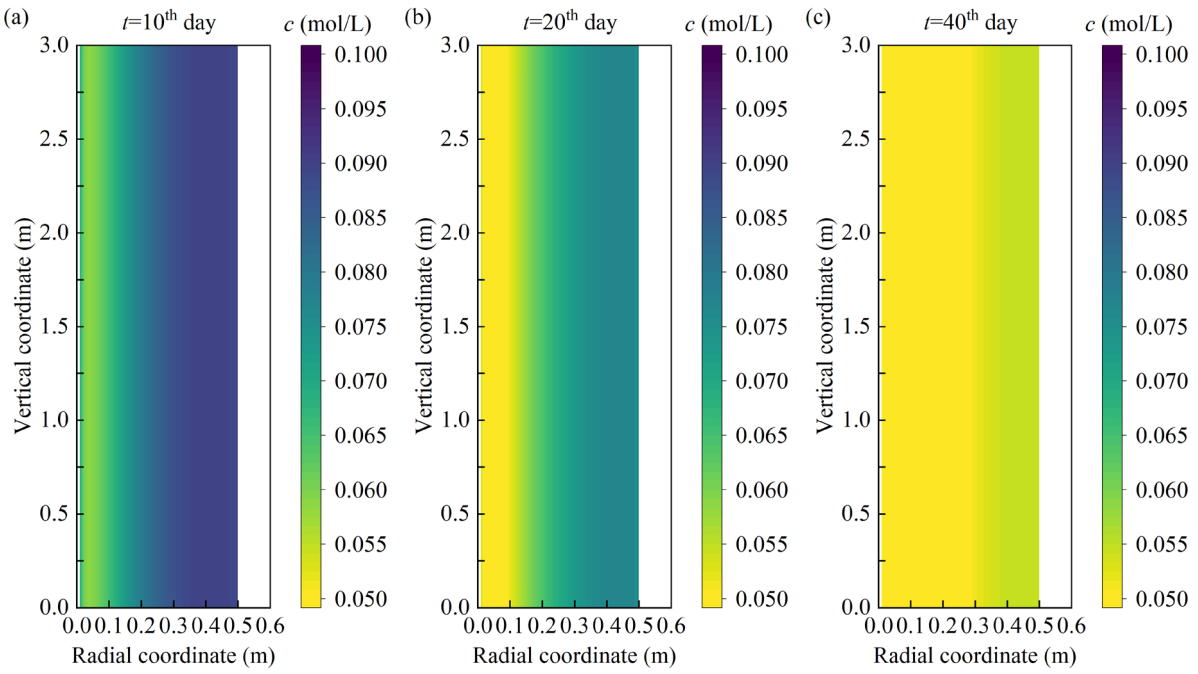

Figure 28 Solute distribution under a vacuum pressure of -20 kPa and a PVD spacing of 0.5 m when K_d=0:

(a) t=10th day, (b) t=20th day, and (c) t=40th day

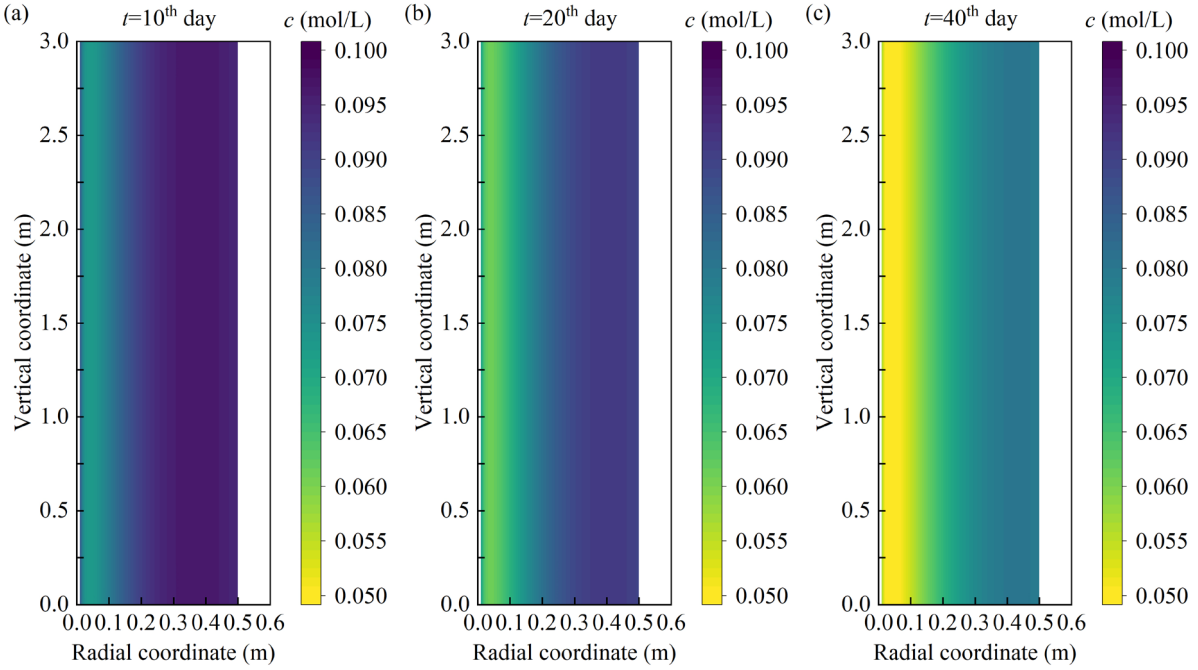

Figure 29 Solute distribution under a vacuum pressure of -20 kPa and a PVD spacing of 0.5 m when K_d=0.2 L/kg: (a) t=10th day, (b) t=20th day, and (c) t=40th day

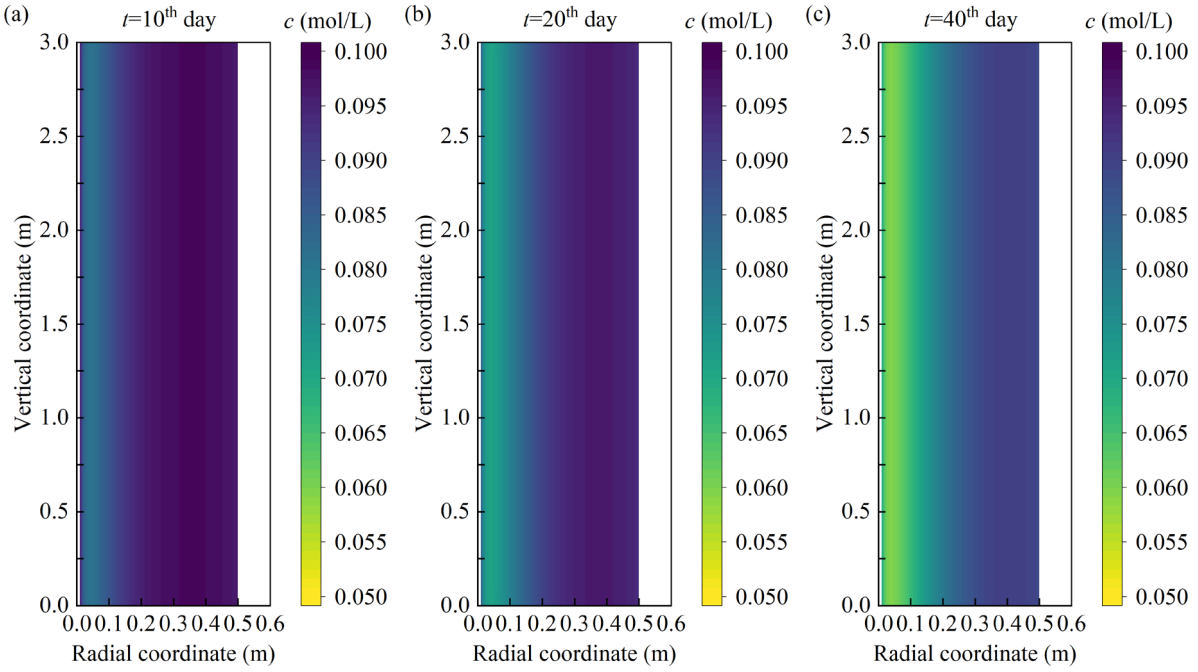

Figure 30 Solute distribution under a vacuum pressure of -20 kPa and a PVD spacing of 0.5 m when K_d=0.4 L/kg: (a) t=10th day, (b) t=20th day, and (c) t=40th day

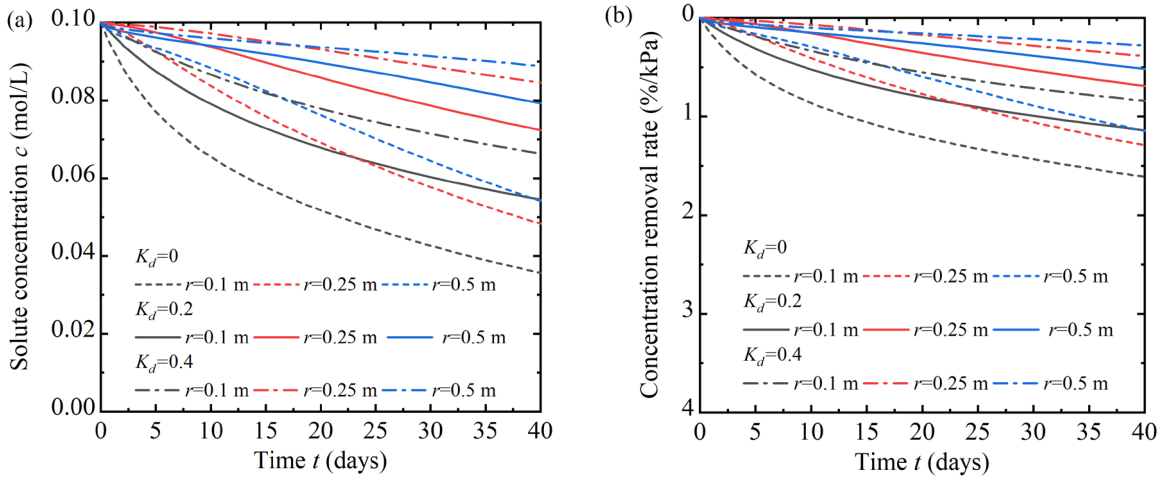

Figure 31 Clean-up effect of different positions under adsorption coefficients: (a) solute concentration, and (b) vacuum-normalized concentration removal rate

6 Discussion

This study proposes a coupled axisymmetric large-strain consolidation–solute transport model that provides a tractable mathematical formulation while capturing the key mechanisms of large strain consolidation and solute transport in PVD-enhanced flushing. For mathematical formulation, The model integrates nonlinear large-strain consolidation using the Yin–Graham EVP model, variable hydraulic conductivity and compressibility, and adsorption effects within a unified axisymmetric PDE framework, and explicitly accounts for radial–vertical coupled flow, creep deformation, and smear zone effects induced by PVD installation. These capabilities overcome the limitations of existing coupled consolidation–solute transport models such as CST2, which is restricted to 1D vertical processes, and flushing analysis models that neglect consolidation effects and realistic vacuum pressure boundaries. To ensure computational efficiency, the proposed model adopts a tailored finite difference scheme with

750 an ADI solution, which improves stability and enables efficient simulation of flushing
751 processes with reduced computational cost. The ADI method has been widely applied in
752 geotechnical engineering to solve 2D coupled problems, including PVD-assisted consolidation
753 (Li et al., 2024), PHD-assisted consolidation (Sun et al., 2023), and large strain consolidation
754 with thermal preloading (Liu et al., 2025), and these successful applications verify its reliability
755 and applicability for solving 2D geotechnical problems. Comparison with CST2 also confirms
756 that the proposed model achieves high accuracy in coupled analysis, with simulation results
757 closely matching those of CST2. Building on this capability, the model is more applicable to
758 field-scale remediation scenarios involving PVD-enhanced flushing of multilayered
759 contaminated soils, where radial consolidation, vacuum loading boundaries, drain spacing,
760 penetration depth, and smear zone effects play critical roles. By restricting analysis to vertical
761 flow, the proposed model reduces to a CST2-type formulation, enabling replication of all
762 scenarios that CST2 can simulate, while its axisymmetric structure and additional field-specific
763 mechanisms allow realistic simulation of more complex site conditions such as combined radial
764 and vertical drainage, coupled solute transport, and engineered drain installations. These
765 enhancements make the proposed approach a more comprehensive and versatile tool for
766 practical engineering design and optimisation of PVD-assisted remediation systems.

767 However, several limitations of the model should be recognized. A key limitation of the
768 present study is the absence of direct validation against full-scale field data for contaminated
769 site remediation. Although considerable time and effort were devoted to searching for relevant
770 datasets in the published literature, no accessible and compatible field data with clearly defined

771 hydro–mechanical–chemical boundary conditions and parameters were found. Consequently,
772 the validation was conducted using well-controlled laboratory-scale experiments on PVD-
773 assisted flushing remediation of contaminated soils, which, despite not being full-scale,
774 successfully captured the essential coupled consolidation–solute transport mechanisms. Future
775 research will focus on collaborating with industry partners to collect high-quality field datasets,
776 enabling comprehensive validation of the proposed model under practical engineering
777 conditions. The proposed model accommodates heterogeneous soil conditions through
778 spatially variable parameter assignment, enabling realistic simulation of multilayered field
779 soils. While dynamic loading, such as cyclic traffic loads, was not investigated herein, it can
780 theoretically be incorporated via a time-dependent total stress function (e.g., $\sigma_z = 100\cos(wt)$).
781 Investigating its influence on coupled consolidation–solute transport is the subject of ongoing
782 research to enhance the field applicability of the proposed model. It also should be noted that
783 the linear adsorption model employed herein may oversimplify the actual sorption behavior of
784 solutes in soils, which is often governed by nonlinear or rate-limited mechanisms. While this
785 assumption facilitates analytical formulation and numerical implementation, future studies are
786 encouraged to incorporate more sophisticated sorption models such as nonlinear isotherms or
787 kinetic formulations to improve the predictive accuracy and broaden the applicability of the
788 framework under realistic field conditions. In addition, from a numerical perspective, the finite
789 difference scheme with an ADI solver has been verified to be stable and convergent for the
790 tested cases. Nevertheless, scenarios involving sharp hydraulic or concentration gradients, or
791 significant material contrasts, may require finer discretization and smaller time steps to

maintain solution accuracy. The accuracy of predictions is mainly affected by the uncertainties in model parameters such as permeability, compressibility, and adsorption coefficients. The current formulation does not explicitly account for complex site conditions including strong heterogeneity, anisotropy, or fissured soils. Chemical reactions and biodegradation effects are not included, which may influence contaminant migration in certain field scenarios.

7 Conclusions

This study aims to advance the analysis of PVD-enhanced flushing in multi-layered contaminated soils by developing an axisymmetric model that couples large strain consolidation with solute transport. The proposed model has been first derived from the large strain consolidation equations, comprehensively incorporating the critical factors influencing PVD-assisted consolidation. Furthermore, the axisymmetric solute transport equation has been derived and seamlessly incorporated into the coupled model. By conducting a comparative analysis involving analytical PVD-assisted flushing models, flushing tests, consolidation-induced tests, and a parametric study, the following conclusions can be drawn:

(a) The study successfully developed a comprehensive axisymmetric model that integrates large strain consolidation with solute transport, specifically designed for evaluating PVD-enhanced flushing in stratified contaminated soils. The model accounts for essential factors affecting consolidation and solute transport processes such as vertical and radial flow, creep, smear zones, nonlinear permeability and compressibility, and vacuum preloading, providing a robust framework for simulating complex soil remediation processes.

(b) The proposed model underwent rigorous validation by being compared with established analytical solutions, PVD-enhanced flushing tests, and consolidation-induced solute transport experiments. The results exhibited strong concordance with both analytical and experimental data, confirming the accuracy and reliability of the proposed model in characterizing the coupled consolidation and solute transport phenomena in multi-layered contaminated soils.

(c) Parametric analyses demonstrated that an increase in vacuum pressure notably accelerates solute migration and enhances cleanup efficiency, especially during the initial phases of remediation. Moreover, minimizing the radial distance between PVDs and optimizing their length further optimize the effectiveness of the remediation process, especially along the radial direction. However, the treatment depth cannot be significantly increased by merely increasing vacuum pressure or reducing the spacing between PVDs.

(d) The performance of the model in simulating real-world conditions, such as variations in vacuum pressures and PVD configurations, makes it an indispensable tool for optimizing soil remediation strategies. As the results indicate, merely increasing vacuum pressures and reducing PVD spacing may not lead to satisfactory remediation outcomes in sites with extensive contamination. In practical engineering applications, a thorough assessment of the spatial distribution of contaminants is essential. This provides valuable insights for engineers and environmental scientists involved in contaminated soil remediation projects.

833 **List of symbols**

a	Lagrangian coordinate
c	solute concentration in the fluid phase
D_{ev}	effective diffusion coefficient in the vertical direction
D_{er}	effective diffusion coefficient in the radial direction
e	void ratio
e_0	initial void ratio
e_{zp}^{ep}	void ratio corresponding to σ'_p
G_s	specific gravity of the soil particle
j	soil layer
k	hydraulic conductivity
k_r	radial hydraulic conductivity
k_s	hydraulic conductivity in smear zone
k_v	vertical hydraulic conductivity
k_{r0}	radial permeability coefficient when e=0
k_{v0}	vertical permeability coefficient when e=0
K_d	adsorption coefficient
M	element number in vertical direction
N	element number in radial direction
n	the soil porosity
n_v	permeability coefficient parameter in vertical direction
n_r	permeability coefficient parameter in radial direction
q	flow flux
q_r	flow flux in the radial direction
q_ξ	flow flux in the vertical direction
r	radial coordinate
r_e	equivalent radius of the influence zone of one vertical drain
r_s	smear zone radius
r_w	vertical drain radius
t	elapsed time
t_0	parameter related to creep
u_e	excess pore water pressure
u_h	hydrostatic pressure
u_w	total pore water pressure

u_{vac}	vacuum pressure value
V	specific volume
v_r	velocity in the radial direction
v_s	velocity of solid phase in the vertical direction
v_w	velocity of fluid phase in the vertical direction
α	permeability reduction ratio in smear zone
γ_m	unit weight of saturated soil
γ_w	unit weight of water
θ	angle coordinate
κ	elastic compression index in the Cam-clay models
λ	elastic-plastic compression index in the Cam-clay models
ξ	Convective coordinate
ρ_s	density of soil particle
ρ_d	dry density of soil
c_s	mass of solute adsorbed on soil particles per unit mass
f	change rate in mass of solute received by the solid phase from the liquid phase
σ	total vertical stress
σ'	effective stress
σ'_p	similar role to the pre-consolidation pressure p_c
σ_{ah}	total stress above hydrostatic pressure
σ'_{ah}	effective stress above hydrostatic pressure
σ'_{ref}	reference effective stress
ψ	creep index

Acknowledgments

The work in this paper is supported by a Research Impact Fund (RIF) project (R5037-18), a Theme-based Research Scheme Fund (TRS) project (T22-502/18-R), and three General Research Fund (GRF) projects (PolyU 152179/18E; PolyU 152130/19E; PolyU 152100/20E) from Research Grants Council (RGC) of Hong Kong Special Administrative Region Government of China. The authors also acknowledge the financial supports from Research Institute for Sustainable Urban Development of The Hong Kong Polytechnic University and a

842 grant ZDBS from The Hong Kong Polytechnic University.

843

844 Data Availability Statement

845 All data that support the findings of this study are available from the corresponding author
846 upon reasonable request.

847

848 Declaration of Competing Interest

849 The authors declare that they have no known competing financial interests or personal
850 relationships that could have appeared to influence the work reported in this paper.

851

852 References

853 Alshawabkeh, A. N., Rahbar, N., Sheahan, T. C., Tang, G., 2004. Volume change effects on
854 solute transport in clay under consolidation. In Geo Jordan 2004: Advances in Geotechnical
855 Engineering with Emphasis on Dams, Highway Materials, and Soil Improvement (pp. 105-
856 115). https://doi.org/10.1061/40735(143)9.

857 Baral, P., Indraratna, B., Rujikiatkamjorn, C., Kelly, R., Vincent, P., 2021. Consolidation by
858 vertical drains beneath a circular Embankment under surcharge and vacuum preloading. J.
859 Geotech. Geoenviron. Eng. 147 (8), 05021004. https://doi.org/10.1061/(ASCE)GT.1943-
860 5606.0002576.

861 Bergado, D. T., Manivannan, R., Balasubramaniam, A. S., 1996. Proposed criteria for

862 discharge capacity of prefabricated vertical drains. Geotext. Geomembr. 14(9), 481-505.
863 https://doi.org/10.1016/S0266-1144(96)00028-3.
864 Bo, M. W., Arulrajah, A., Horpibulsuk, S., Chinkulkijniwat, A., Leong, M., 2016. Laboratory
865 measurements of factors affecting discharge capacity of prefabricated vertical drain
866 materials. Soil. Found. 56(1), 129-137. https://doi.org/10.1016/j.sandf.2016.01.010.
867 Chai, J. C., Carter, J. P., Hayashi, S., 2005. Ground deformation induced by vacuum
868 consolidation. J. Geotech. Geoenviron. Eng. 131 (12), 1552-1561.
869 https://doi.org/10.1061/(ASCE)1090-0241(2005)131:12(1552).
870 Chu, J., Bo, M., Choa, V., 2006. Improvement of ultra-soft soil using prefabricated vertical
871 drains. Geotext. Geomembr. 24 (6), 339-348.
872 https://doi.org/10.1016/j.geotexmem.2006.04.004.
873 Chu, J., Yan, S. W., Yang, H., 2000. Soil improvement by the vacuum preloading method for
874 an oil storage station. Géotechnique. 50 (6), 625-632.
875 https://doi.org/10.1680/geot.2000.50.6.625.
876 Fox, P. J., 2007. Coupled large strain consolidation and solute transport. I: Model development.
877 J. Geotech. Geoenviron. Eng. 133(1), 3-15. https://doi.org/10.1061/(ASCE)1090-
878 0241(2007)133:1(3).
879 Fox, P. J., Di Nicola, M., Quigley, D. W., 2003. Piecewise-linear model for large strain radial
880 consolidation. J. Geotech. Geoenviron. Eng. 129(10), 940-950.
881 https://doi.org/10.1061/(ASCE)1090-0241(2003)129:10(940).
882 Fox, P. J., Lee, J., 2008. Model for consolidation-induced solute transport with nonlinear and

883 nonequilibrium sorption. Int. J. Geomech. 8(3), 188-198.
884 https://doi.org/10.1061/(ASCE)1532-3641(2008)8:3(188).
885 Gabr, M. A., Bowders, J. J., Wang, J., Quaranta, J., 1996a. In situ soil flushing using
886 prefabricated vertical drains. Can. Geotech. J. 33(1), 97-105. https://doi.org/10.1139/t96-
887 026.
888 Gabr, M. A., Wang, J., Bowders, J. J., 1996b. Model for efficiency of soil flushing using PVD-
889 enhanced system. J. Geotech. Eng. 122(11), 914-919.
890 https://doi.org/10.1061/(ASCE)0733-9410(1996)122:11(914).
891 Geng, X., Yu, H. S., 2017. A large-strain radial consolidation theory for soft clays improved
892 by vertical drains. Géotechnique. 67(11), 1020-1028.
893 Gibson, R. E., England, G. L., Hussey, M. J. L., 1967. The theory of one-dimensional
894 consolidation of saturated clays: 1. Finite non-linear consolidation of thin homogeneous
895 layers. Géotechnique. 17(3), 261-273. https://doi.org/10.1680/geot.1967.17.3.261.
896 Gibson, R. E., Schiffman, R. L., Cargill, K. W., 1981. The theory of one-dimensional
897 consolidation of saturated clays. II. Finite nonlinear consolidation of thick homogeneous
898 layers. Can. Geotech. J. 18(2), 280-293. https://doi.org/10.1139/t81-030.
899 Huangfu, Z., Deng, A., 2024. Vertical drain aided consolidation and solute transport. Comput.
900 Geotech. 166, 106050. https://doi.org/10.1016/j.compgeo.2023.106050.
901 Indraratna, B., Rujikiatkamjorn, C., Kelly, R., Buys, H., 2012. Soft soil foundation improved
902 by vacuum and surcharge loading. Proc. Inst. Civ. Eng.: Gr. Improv. 165 (2), 87-96.
903 https://doi.org/10.1680/grim.10.00032.

Jiang, L., Qin, A., Li, L., Meng, H., Xu, W., 2024. Prediction models for effective PVD-enhanced in-situ flushing remediation of multi-layered soils. Comput. Geotech. 166, 106022. https://doi.org/10.1016/j.compgeo.2023.106022.

Jiang, L., Qin, A., Li, L., Tang, P., 2023. Approximate analytical solution to the axisymmetric model for PVD-enhanced in-situ flushing of double-layered contaminated soils. Comput. Geotech. 161, 105619. https://doi.org/10.1016/j.compgeo.2023.105619.

Jiang, W., Ge, S., Feng, C., Huang, X., Li, J. 2023. Coupled model for one‐dimensional nonlinear consolidation and organic contaminant transport in a triple‐layer composite liner considering the nonisothermal distribution condition. Int. J. Numer. Anal. Methods Geomech. 47(10), 1772-1801. https://doi.org/10.1002/nag.3538.

Lee, J., Fox, P. J., 2009. Investigation of consolidation-induced solute transport. II: Experimental and numerical results. J. Geotech. Geoenviron. Eng. 135(9), 1239-1253. https://doi.org/10.1061/(ASCE)GT.1943-5606.0000048.

Lee, J., Fox, P. J., Lenhart, J. J., 2009. Investigation of consolidation-induced solute transport. I: Effect of consolidation on transport parameters. J. Geotech. Geoenviron. Eng. 135(9), 1228-1238. https://doi.org/10.1061/(ASCE)GT.1943-5606.0000047.

Li, J., Jiang, W., Ge, S., Feng, C., Huang, X., Wang, P. 2022. Coupled model for consolidation and organic contaminant transport in GMB/CCL composite liner under non-isothermal distribution condition. Comput. Geotech. 150, 104893. https://doi.org/10.1016/j.compgeo.2022.104893.

Li, P. L., Song, D. B., Yin, Z. Y., Yin, J. H. 2025. Large strain consolidation model for very

soft soils with prefabricated horizontal drains considering nonlinear compression and creep. Acta. Geotech. 20, 1431-1453. https://doi.org/10.1007/s11440-024-02452-3.

Li, P. L., Yin, Z. Y., Song, D. B., Yin, J. H., Pan, Y., 2024. Axisymmetric finite strain consolidation model for soft soil consolidation with vertical drains under combined loading considering creep and non-Darcy flow. Geotext. Geomembr. 52(3), 241-259.

Li, P., Yin, J. H., Yin, Z. Y., Chen, Z., 2023. One-dimensional nonlinear finite strain analysis of self–weight consolidation of soft clay considering creep. Comput. Geotech. 153, 105081. https://doi.org/10.1016/j.compgeo.2022.105081.

Liu, Y., Wu, P., Li, P., Yin, J. H., Zheng, J. J., 2025. Fully coupled large-strain radial consolidation analysis for dredged marine slurry treated by prefabricated vertical drain with vacuum and heat preloading. Comput. Geotech. 177, 106852.

Miura, N., Chai, J. C., 2000. Discharge capacity of prefabricated vertical drains confined in clay. Geosynth. Int. 7(2), 119-135. https://doi.org/10.1680/gein.7.0169.

Nassar, I. N., Horton, R., 1992. Simultaneous transfer of heat, water, and solute in porous media: I. Theoretical development. Soil Sci. Soc. Am. J. 56(5), 1350-1356. https://doi.org/10.2136/sssaj1992.03615995005600050004x.

Nguyen, B. P., Kim, Y. T., 2019. Radial consolidation of PVD-Installed normally consolidated soil with discharge capacity reduction using large-strain theory. Geotext. Geomembr. 47(2), 243-254. https://doi.org/10.1016/j.geotexmem.2019.01.008.

Nomura, S., Kawai, K., Tachibana, S., Iizuka, A., 2018. Solute transfer during consolidation based on a solid-fluid-solute coupling model. Int. J. Numer. Anal. Methods Geomech.

946 26(10), 1172-1196. https://doi.org/10.1002/nag.2787.
947 Park, J., Shin, E., 2009. Applicability of soil flushing remediation system for contaminated
948 fine-grained soils using PVDs. Int J Geotech Eng. 3(3), 417-427.
949 https://doi.org/10.3328/IJGE.2009.03.03.417-427.
950 Peaceman, D. W., Rachford, H. H., 1955. The numerical solution of parabolic and elliptic
951 differential equations. J. Soc. Ind. Appl. Math. 3 (1), 28-41.
952 https://doi.org/10.1137/0103003.
953 Peters, G. P., Smith, D. W., 2002. Solute transport through a deforming porous medium. Int. J.
954 Numer. Anal. Methods Geomech. 26(7), 683-717. https://doi.org/10.1002/nag.219.
955 Potter, L. J., Savvidou, C., Gibson, R. E., 1994. Consolidation and pollutant transport
956 associated with slurried mineral waste disposal. In International congress on environmental
957 geotechnics (pp. 525-530).
958 Prabavathy, S., Rajagopal, K., Pitchumani, N. K., 2021. Investigation of smear zone around
959 PVD mandrel using image-based analysis. Int. J. Geosynth. Ground Eng. 7, 1-16.
960 https://doi.org/10.1007/s40891-021-00337-z.
961 Pu, H., Fox, P. J., 2016. Model for coupled large strain consolidation and solute transport in
962 layered soils. Int. J. Geomech. 16(2), 04015064. https://doi.org/10.1061/(ASCE)GM.1943-
963 5622.000053.
964 Pu, H., Wang, K., Qiu, J., Chen, X., 2020. Large-strain numerical solution for coupled self-
965 weight consolidation and contaminant transport considering nonlinear compressibility and
966 permeability. Appl. Math. Model. 88, 916-932. https://doi.org/10.1016/j.apm.2020.07.010.

967 Quaranta, J. D., Kunberger, T., Gabr, M. A., 2005. WIDE application for subsurface hydraulic
968 head control. In Waste Containment and Remediation (pp. 1-12).
969 Sharmin, N., Kunberger, T., Gabr, M. A., Quaranta, J. D., Bowders, J. J., 2008. Performance
970 modeling and optimization of contaminant extraction using prefabricated vertical wells
971 (PVWs). Geosynth. Int. 15(3), 205-215. https://doi.org/10.1680/gein.2008.15.3.205.
972 Sun, H. L., Zhang, H., Geng, X. Y., Cui, Y. J., Cai, Y. Q., 2023. Large-strain consolidation
973 analysis for clayey sludge improved by horizontal drains. J. Geotech. Geoenviron.
974 Eng.149(8), 04023057.
975 Tang, X. W., Wang, H. Y., Wang, Y., Tang, Q., Gan, P. L., 2015. An analytical solution for
976 contaminant extraction using well injection depth extraction technology. Geotext.
977 Geomembr. 43(2), 118-127. https://doi.org/10.1016/j.geotexmem.2014.12.002.
978 Walker, R., Indraratna, B., 2006. Vertical drain consolidation with parabolic distribution of
979 permeability in smear zone. J. Geotech. Geoenviron. Eng. 132(7), 937-941.
980 https://doi.org/10.1061/(ASCE)1090-0241(2006)132:7(937).
981 Wang, H. Y., Tang, X. W., Gan, P. L., 2014. Analytical solution for contaminant extraction
982 using well injection depth extraction technology considering the effect of smear zone. Appl.
983 Mech. Mater. 580, 560-565. https://doi.org/10.4028/www.scientific.net/AMM.580-
984 583.560.
985 Wang, H. Y., Tang, X. W., Tang, Q., Wang, Y., Gan, P. L., 2016. An analytical solution for
986 contaminant extraction in a radial flow field using PVD-enhanced system. Geosynth. Int.
987 23(1), 23-35. https://doi.org/10.1680/gein.15.00029.

988 Wu, Y., Yue, H., Zhang, X., Zang, X., Sun, Y., Zhang, C., Chau, N. X. Q., 2024. Research on
989 the heavy metal migration and distribution patterns of low permeability copper and zinc
990 contaminated soil during bottom vacuum leaching. Process Safety and Environmental
991 Protection. https://doi.org/10.1016/j.psep.2024.04.017.
992 Xie, H., Yan, H., Feng, S., Wang, Q., Chen, P., 2016. An analytical model for contaminant
993 transport in landfill composite liners considering coupled effect of consolidation, diffusion,
994 and degradation. Environ. Sci. Pollut. Res. 23, 19362-19375.
995 https://doi.org/10.1007/s11356-016-7147-6.
996 Yin, J. H., Graham, J., 1989. Viscous-elastic-plastic modelling of one-dimensional time-
997 dependent behaviour of clays. Can. Geotech. J. 26(2), 199-209. https://doi.org/10.1139/t89-
998 029.
999 Yin, J. H., Graham, J., 1994. Equivalent times and one-dimensional elastic viscoplastic
1000 modelling of time-dependent stress–strain behaviour of clays. Can. Geotech. J. 31(1), 42-
1001 52. https://doi.org/10.1139/t94-005.
1002 Yin, J. H., Graham, J., 1996. Elastic visco-plastic modelling of one-dimensional consolidation.
1003 Géotechnique. 46(3), 515-527. https://doi.org/10.1680/geot.1996.46.3.515.
1004 Yin, J. H., Zhu, G., 2020. Consolidation analyses of soils. CRC Press.
1005 Zhang, Z., Tian, G., Song, Z., 2025. The influence of fixed charges on chemo–hydro–
1006 mechanical coupled behavior of saturated soil layer. Comput. Geotech. 179, 107000.
1007 https://doi.org/10.1016/j.compgeo.2024.107000.
1008

Appendix A

The finite difference scheme of Equation (41) can be obtained in the following procedures. Firstly, Equation (41) can be expressed as below:

$$A_5\frac{\partial u_e}{\partial t}=A_1\frac{\partial u_e^2}{\partial r^2}+A_2A_3\frac{\partial u_e^2}{\partial a^2}+\frac{A_1}{r}\frac{\partial u_e}{\partial r}+\frac{\partial A_1}{\partial r}\frac{\partial u_e}{\partial r}+A_3\frac{\partial A_2}{\partial a}\frac{\partial u_e}{\partial a}+A_4 \tag{A1}$$

The Peaceman-Rachford (P-R) ADI scheme of Equation (A1) consists of solving the equation implicitly in the *r*-direction and explicitly in the *a*-direction for time $t+\Delta t/2$ is expressed as follow:

$$\begin{aligned}&\left(A_5\right)_{I,J}^{t}\frac{2}{\Delta t}\left(u_{eI,J}^{t+\Delta t/2}-u_{eI,J}^{t}\right)\\&=\left(A_1\right)_{I,J}^{t}\left(\frac{u_{eI,J+1}^{t+\Delta t/2}-2u_{eI,J}^{t+\Delta t/2}+u_{eI,J-1}^{t+\Delta t/2}}{\Delta r^2}\right)+\frac{\left(A_1\right)_{I,J}^{t}}{r}\left(\frac{u_{eI,J+1}^{t+\Delta t/2}-u_{eI,J}^{t+\Delta t/2}}{2\Delta r}\right)\\&+\left(\frac{\partial A_1}{\partial r}\right)_{i,j}^{t}\left(\frac{u_{eI,J+1}^{t+\Delta t/2}-u_{eI,J}^{t+\Delta t/2}}{2\Delta r}\right)+\left(A_2A_3\right)^{t}\left(\frac{u_{eI+1,J}^{t}-2u_{eI,J}^{t}+u_{eI-1,J}^{t}}{\Delta a^2}\right)+\left(A_3\frac{\partial A_2}{\partial a}\right)_{I,J}^{t}+\left(A_4\right)_{I,J}^{t}\end{aligned} \tag{A2}$$

Implicitly in the *a*-direction and explicitly in the *r*-direction for time $t+\Delta t$, one can rewrite Equation (A1):

$$\begin{aligned}&\left(A_5\right)_{I,J}^{t}\frac{2}{\Delta t}\left(u_{I,J}^{t+\Delta t}-u_{I,J}^{t+\Delta t/2}\right)\\&=\left(A_1\right)_{I,J}^{t}\left(\frac{u_{I,J+1}^{t+\Delta t/2}-2u_{I,J}^{t+\Delta t/2}+u_{I,J-1}^{t+\Delta t/2}}{\Delta r^2}\right)+\frac{\left(A_1\right)_{I,J}^{t}}{r}\left(\frac{u_{I,J+1}^{t+\Delta t/2}-u_{I,J}^{t+\Delta t/2}}{2\Delta r}\right)\\&+\left(\frac{\partial A_1}{\partial r}\right)_{I,J}^{t}\left(\frac{u_{I,J+1}^{t+\Delta t/2}-u_{I,J}^{t+\Delta t/2}}{2\Delta r}\right)+\left(A_2A_3\right)_{I,J}^{t}\left(\frac{u_{I+1,J}^{t+\Delta t}-2u_{I,J}^{t+\Delta t}+u_{I-1,J}^{t+\Delta t}}{\Delta a^2}\right)+\left(A_3\frac{\partial A_2}{\partial a}\right)_{I,J}^{t}+\left(A_4\right)_{I,J}^{t}\end{aligned} \tag{A3}$$

where:

$$\left(A_1\right)_{I,J}^{t}=\frac{k_{r0}\left(1+e_{I,J}^{t}\right)^{n_r}}{\gamma_w} \tag{A4}$$

1022
$$\left(\frac{\partial A_1}{\partial r}\right)_{I,J}^{t}=\frac{n_r k_{r0}\left(1+e_{I,J}^{t}\right)^{n_r-1}}{\gamma_w}\frac{e_{I,J+1}^{t}-e_{I,J}^{t}}{\Delta r} \tag{A5}$$

1023
$$\left(A_2A_3\right)_{I,J}^{t}=\frac{\left(1+e_0\right)^2 k_{v0}\left(1+e_{I,J}^{t}\right)^{n_v-2}}{\gamma_w} \tag{A6}$$

1024
$$\left(A_3\frac{\partial A_2}{\partial a}\right)_{I,J}^{t}=\frac{k_{v0}\left(1+e_0\right)\left(n_v-1\right)\left(1+e_{I,J}^{t}\right)^{n_v-2}}{\gamma_w}\left(\frac{e_{I+1,J}^{t}-e_{I,J}^{t}}{\Delta a}\right) \tag{A7}$$

1025 Equations (A2) can further transferred into

1026
$$u_{eI,J}^{t+\Delta t/2}=E^{\mathrm{I}}+E^{\mathrm{II}}u_{eI,J+1}^{t+\Delta t/2}+E^{\mathrm{III}}u_{eI,J-1}^{t+\Delta t/2} \tag{A8}$$

1027 Then for each *I*, we can obtain a tridiagonal matrix

1028
$$\begin{bmatrix} 1 & -E_{I,1}^{\mathrm{II}} & 0 & & & \\ -E_{I,2}^{\mathrm{III}} & 1 & -E_{I,2}^{\mathrm{II}} & & & \\ 0 & -E_{I,3}^{\mathrm{III}} & 1 & -E_{I,3}^{\mathrm{II}} & & \\ \vdots & & & \ddots & & \\ & & & -E_{I,N-3}^{\mathrm{III}} & 1 & -E_{I,N-3}^{\mathrm{II}} \\ & & & & -E_{I,N-2}^{\mathrm{III}} & 1-E_{I,N-2}^{\mathrm{II}} \end{bmatrix}\begin{bmatrix} u_{eI,2} \\ u_{eI,3} \\ u_{eI,4} \\ \vdots \\ u_{eI,N-2} \\ u_{eI,N-1} \end{bmatrix}^{t+\frac{\Delta t}{2}}=\begin{bmatrix} E_{I,1}^{\mathrm{I}}+E_{I,1}^{\mathrm{III}}u_{eI,1}^{t+\Delta t/2} \\ E_{I,2}^{\mathrm{I}} \\ E_{I,3}^{\mathrm{I}} \\ \vdots \\ E_{I,N-3}^{\mathrm{I}} \\ E_{I,N-2}^{\mathrm{I}} \end{bmatrix} \tag{A9}$$

1029 where:

1030
$$E^{\mathrm{I}}=\frac{\left(A_2A_3\right)_{I,J}^{t}\left(u_{eI+1,J}^{t}-2u_{eI,J}^{t}+u_{eI-1,J}^{t}\right)+\Delta a^2\left(A_3\partial A_2/\partial a\right)_{I,J}^{t}+2\Delta t\Delta a^2\left[\left(A_4\right)_{I,J}^{t}+u_{eI,J}^{t}\right]}{2\Delta t\Delta a^2E^0\left(A_5\right)_{I,J}^{t}} \tag{A10}$$

1031
$$E^{\mathrm{II}}=E^{\mathrm{III}}=\frac{\Delta t\left[2r\left(A_1\right)_{I,J}^{t}+\Delta r\left(A_1\right)_{I,J}^{t}+r\Delta r\left(\partial A_1/\partial r\right)_{I,J}^{t}\right]}{4r\Delta r^2E^0} \tag{A11}$$

1032
$$E^0=\left(A_5\right)_{I,J}^{t}+\Delta t\left(A_1\right)_{I,J}^{t}/\Delta r^2 \tag{A12}$$

1033 Similarly, Equation (A3) can be rewritten as

1034
$$u_{eI,J}^{t+\Delta t}=F^{\mathrm{I}}+F^{\mathrm{II}}u_{eI+1,J}^{t+\Delta t}+F^{\mathrm{III}}u_{eI-1,J}^{t+\Delta t} \tag{A13}$$

1035 For each *J*, one can obtain

1036
$$\begin{bmatrix} 1 & -F^{\mathrm{II}}_{2,J} & 0 & & & \\ -F^{\mathrm{III}}_{3,J} & 1 & -F^{\mathrm{II}}_{3,J} & & & \\ 0 & -F^{\mathrm{III}}_{4,J} & 1 & & & \\ \vdots & & & \ddots & & \\ & & & -F^{\mathrm{III}}_{N-2,J} & 1 & -F^{\mathrm{II}}_{N-2,J} \\ & & & & -F^{\mathrm{III}}_{N-1,J} & 1-F^{\mathrm{II}}_{N-1,J} \end{bmatrix} \begin{bmatrix} u_{e2,J} \\ u_{e3,J} \\ u_{e4,J} \\ \vdots \\ u_{eN-2,J} \\ u_{eN-1,J} \end{bmatrix}^{t+\Delta t} = \begin{bmatrix} F^{\mathrm{I}}_{1,J} + F^{\mathrm{III}}_{1,J} u^{t+\Delta t}_{e1,J} \\ F^{\mathrm{I}}_{2,J} \\ F^{\mathrm{I}}_{3,J} \\ \vdots \\ F^{\mathrm{I}}_{N-2,J} \\ F^{\mathrm{I}}_{N-3,J} \end{bmatrix} \quad \text{(A14)}$$

1037 where:

1038
$$F^{\mathrm{I}} = \left[\frac{2}{\Delta t} - \frac{2\left(A_1\right)^t_{i,j}}{\Delta r^2} \right] u^{t+\Delta t/2}_{eI,J} + \left[\frac{\left(A_1\right)^t_{I,J}}{\Delta r^2} + \frac{\left(A_1\right)^t_{I,J}}{2r\Delta r} \left(\frac{\partial A_1}{\partial r} \right)^t_{I,J} \frac{1}{2\Delta r} \right] \left(u^{t+\Delta t/2}_{eI,J+1} + u^{t+\Delta t/2}_{eI,J-1} \right) + \left(A_3 \frac{\partial A_2}{\partial a} \right)^t_{I,J} + \left(A_4\right)^t_{I,J} \quad \text{(A15)}$$

1039
$$F^{\mathrm{II}} = F^{\mathrm{III}} = \left(A_2 A_3\right)^t_{I,J} / \left(F^0 \Delta a^2\right) \quad \text{(A16)}$$

1040
$$F^0 = 2/\Delta t + 2\left(A_2 A_3\right)^t_{I,J} / \Delta a^2 \quad \text{(A17)}$$